Geological Quarterly, 2026, 70, 13
DOI: https://doi.org/10.7306/gq.1858

Astronomical forcing of Lower Cretaceous deep-marine turbidites in the Outer Western Carpathians (southern Poland)

Agata KUŹMA[1, *], Krzysztof NINARD[2] and Alfred UCHMAN[2]

[1] Jagiellonian University, Doctoral School of Exact and Natural Sciences, Institute of Geological Sciences, Gronostajowa 3a, 30-387 Kraków, Poland); ORCID: 0000-0003-3821-0911

[2] Jagiellonian University, Institute of Geological Sciences, Gronostajowa 3a, 30-387 Kraków, Poland; ORCID: 0000-0002-7260-5979 [K.N.], 0000-0002-0591-777X [A.U.]

Kuźma, A., Ninard, K., Uchman, A., 2026. Astronomical forcing of Lower Cretaceous deep-marine turbidites in the Outer Western Carpathians (southern Poland). Geological Quarterly, **70**, 13; https://doi.org/10.7306/gq.1858

Deep-marine turbiditic systems are controlled by the supply of terrigenous material and are predominantly influenced by autocyclic processes related to channel migration or lobe switching. Despite advances in understanding cyclic sedimentary successions linked to orbital forcing, research on orbital cycles in deep-marine, turbiditic sequences remains rare. This study examines the relationship between terrigenous material supply and astronomical forcing, offering insights into the timing and mechanisms of turbidite deposition in the Lower Cretaceous deep-marine deposits of the Alpine thrust-and-fold belt, Outer Western Carpathians in southern Poland. The 220 m log investigated from the Krzyworzeka river section at Poznachowice Górne was analysed using a general lithological log treated as a time series. A series of statistical tests assessed whether lithological variations were random, influenced by deterministic processes, or showed cyclicity. The results reveal a strong correlation between sedimentary patterns and climate oscillations driven by precession, obliquity, and eccentricity, with short eccentricity and obliquity modulation exerting the strongest influence. Combining four independent cyclostratigraphic methods allowed identification of recurring trends in bed thickness across five well-defined turbiditic facies. These findings provide new insights into the role of astronomical forcing in controlling deep-marine sedimentation and highlight the new, advanced statistical approaches such as multi-channel singular spectrum analysis, and recurrence plots, in reconstructing past climate dynamics.

Key words: Milankovitch cycles, deep-marine clastics, turbidites, orbital forcing, sedimentology.

INTRODUCTION

Deep-marine turbiditic systems are controlled by terrigenous supply and typically influenced by autocyclic processes (e.g., channel migration, lobe switching), tectonics, and intermittent erosion. Incomplete sedimentary records commonly obscure signals of orbitally forced processes (Postma et al., 1993). Research on orbital cycles in turbiditic sequences is limited, despite advances in understanding cyclic sedimentary successions in shallow-marine and hemipelagic deposits (e.g., Liu et al., 2024; Zhang et al., 2025). Studies of turbiditic environments usually emphasise the effects of other controlling mechanisms such as tectonics (Postma et al., 1993), though some outcrops show clear orbital cyclicity (Foucault et al., 1987; Haak and Schlager, 1989; Postma et al., 1993; Ten Kate and Sprenger, 1993; Weltje and de Boer, 1993; Reijmer et al., 1994; Krijgsman et al., 1999; Pickering et al., 1999; Heard et al., 2008; Mawson and Tucker, 2009; Pickering and Bayliss, 2009; Sutcliffe and Pickering, 2009; Di Celma, 2011; Di Celma and Cantalamessa, 2012; Payros and Martínez-Braceras, 2014; Cantalejo and Pickering, 2015; Cantalejo et al., 2021; Payros et al., 2023).

Detecting orbital cycles provides insight into environmental dynamics and climatic forcing in deep-marine environments. Postma et al. (1993) linked turbiditic deposition in a Miocene submarine fan-lobe from Gavdos (Greece) to precession cycles through visual observations and qualitative analyses. Weltje and de Boer (1993) demonstrated that the temporal evolution of Pliocene fan lobes on Corfu aligned with precession, with sediment supply responding to precipitation and continental runoff. Ten Kate and Sprenger (1993) identified long eccentricity signals in Upper Cretaceous Betic Cordilleras turbidites, and Milankovitch cycles (obliquity and eccentricity) were documented in Eocene Spanish Pyrenees deposits (Heard et al., 2008; Pickering and Bayliss, 2009; Sutcliffe and Pickering, 2009; Cantalejo and Pickering, 2015; Cantalejo et al., 2021). Payros and Martínez-Braceras (2014) linked turbidite frequency and energy to hemi-precession cycles, showing that peak activity during maximum eccentricity and boreal summer coincided with perihelion, resulting in pronounced seasonality, heavy summer rainfall, and the inverse effects during other orbital phases, further detecting precession, obliquity, and eccentricity influences in the sequence (Payros et al., 2023). Examples include Maastrichtian turbidites in Italy (Foucault et al.,

* Corresponding author, e-mail: aga.kuzma@doctoral.uj.edu.pl

Received: January 28, 2026; accepted: April 18, 2026; first published online: May 15, 2026

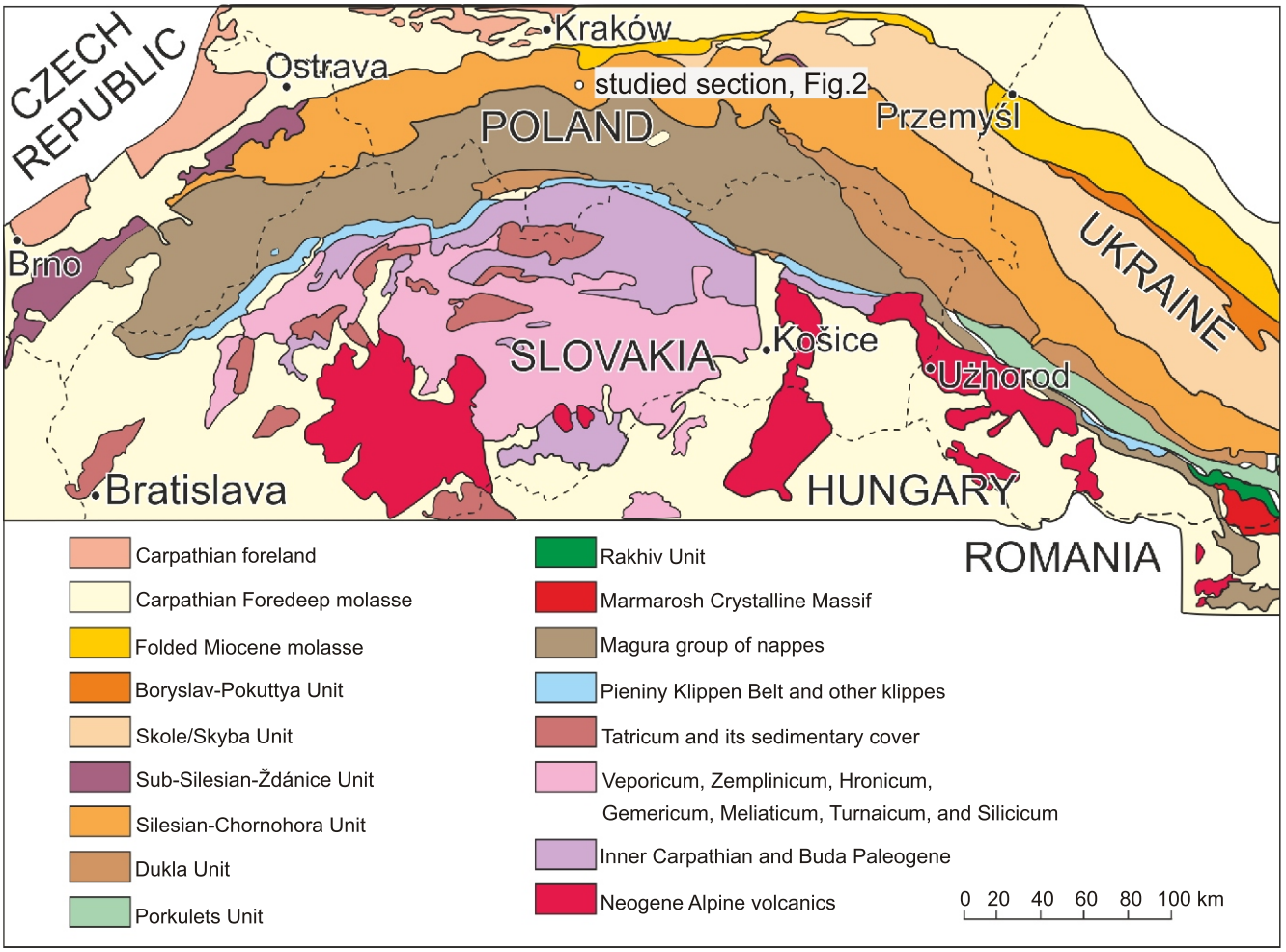

Fig. 1. A simplified map of the Northern Carpathians (after Oszczypko, 2004)

The section studied is located within the Silesian-Chornohora Unit

1987), Triassic calciturbidites in Austria (Reijmer et al., 1994), Miocene Moroccan turbidites (Krijgsman et al., 1999), and Permian deposits in England (Mawson and Tucker, 2009), with additional Pleistocene cases (e.g., Haak and Schlager, 1989; Pickering et al., 1999; Di Celma, 2011; Di Celma and Cantalamessa, 2012).

This study examines lithological changes and orbital influences in Lower Cretaceous (Valanginian) deep-marine deposits of the Outer Western Carpathians (Fig. 1), aiming to clarify the timing and mechanisms of turbiditic deposition. Many aspects of Carpathian evolution remain unresolved and unexamined using numerical techniques. Leszczyński (1997) correlated lithological and geochemical changes in the Sub-Menilite Globigerina Marl with short eccentricity and obliquity. These conclusions were drawn from stratigraphic data and sedimentation rate estimations but are not supported by numerical techniques. The Globigerina Marl is generally interpreted as a pelagic to hemipelagic deposit rather than a turbiditic succession.

Statistical analysis of the Carpathian Flysch is limited by small, isolated exposures; however, the Krzyworzeka river section, with Lower Cretaceous deposits, is an exception. Detailed "bed-by-bed" logging and statistical analyses enable interpretation of both the timing and mechanisms of deposition in this unique geological setting.

GEOLOGICAL SETTING

LOCATION AND GENERAL STRATIGRAPHY

The Krzyworzeka river section is located in the Outer Western Carpathians, Silesian Unit (Fig. 1), near Poznachowice Górne, Poland, extending along the river for a distance of 1700 m (N49°49'20.80", E20°7'8.738" to N49°50'7.43", E20°7'3.759"; Fig. 2). The Outer Western Carpathians are a classical area for deep-marine sedimentology, palaeogeography, ichnology, and micropalaeontology (e.g., Książkiewicz, 1954, 1956; Dżułyński et al., 1959; Dżułyński and Walton, 1963; Geroch and Nowak, 1984; Uchman, 1998).

The Silesian Unit (Silesian-Chornohora Unit; Oszczypko, 2004) extends from the Western to the Eastern Carpathians and records continuous deep-marine sedimentation from the Kimmeridgian to the Miocene. The Valanginian–Hauterivian Upper Cieszyn Beds (~300 m) consist of very thin- to thin-bedded dark grey-black marly mudstones interbedded with fine-grained, cross-laminated calcareous sandstones, sideritic claystones, and mudstones. The sandstones have sharp, erosive bases and gradational tops, forming turbidite sandstone-mudstone couplets capped by hemipelagic mudstones (cf. C2.3 facies of Pickering et al., 1986), though the turbiditic

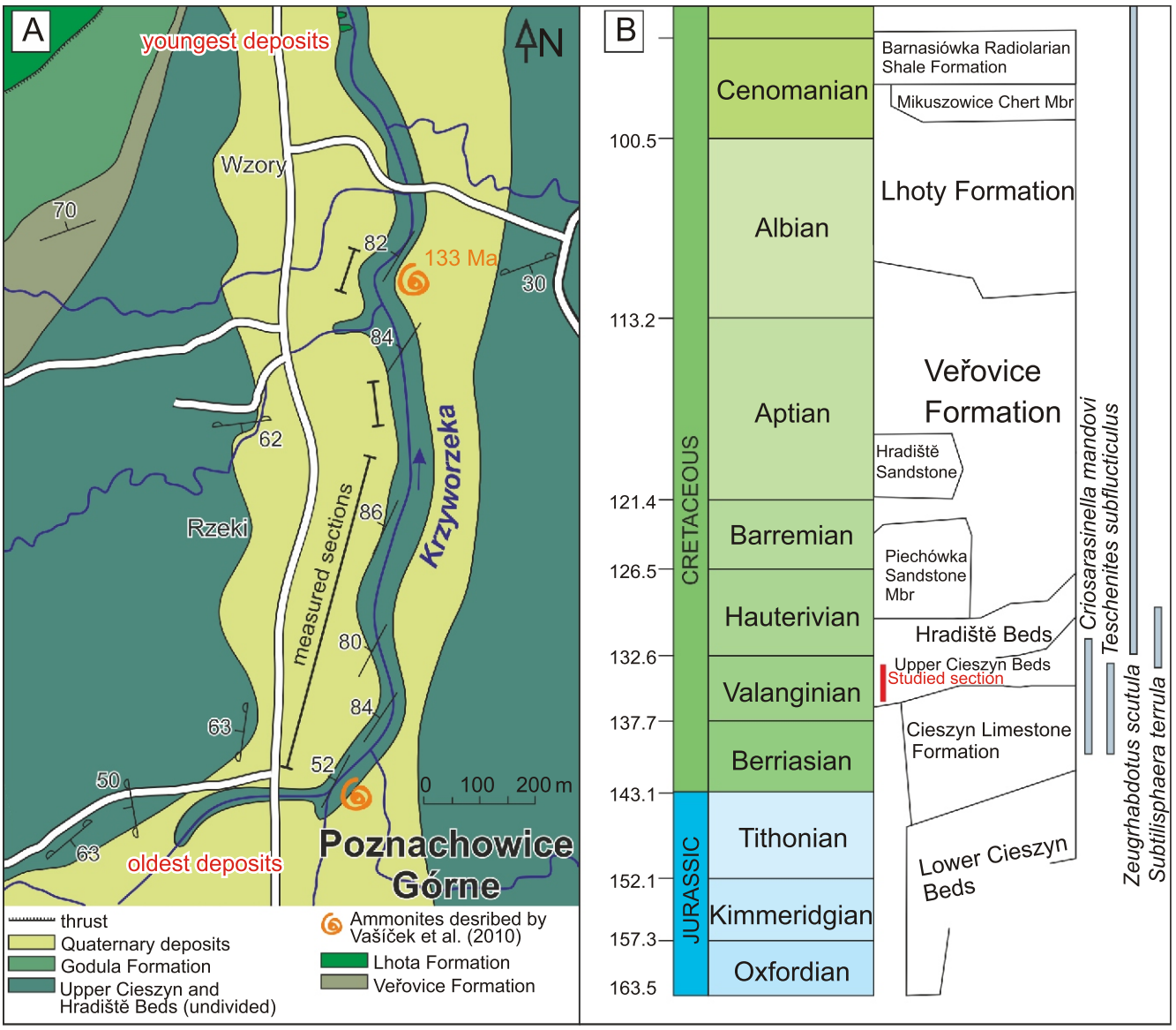

Fig. 2. Geological map of the section studied (after Uchman et al., 2023), the measured section is indicated (A), stratigraphy of the Silesian Unit. Modified after: Geroch (1966), Szymakowska (1981), Ślączka et al. (2006), Olszewska et al. (2008), Vašíček et al. (2010), Mutterlose et al. (2021) in the context of biostratigraphic data from the Krzyworzeka River section (Vašíček et al., 2010; Kędzierski and Ochabska, 2012, with reinterpretation in this paper; B)

and locally hemipelagic mudstone layers are thicker here (Uchman and Szczęch, 2022). Turbidity currents transported material from the north-west, which was deposited above the CCD. The overlying Hradište Beds (~140 m) comprise dark-grey, marly shales with thin-bedded, fine-grained sandstones and sideritic beds, locally including coarse-grained sandstones and conglomerates with exotic clasts (Uchman, 2008). Both units were deposited in the Proto-Silesian Basin (part of the Severin-Moldavidic Basin), dominated by calcareous sediments. The basin developed as a rift-related back-arc system along the northern margin of the European Platform, bounded to the south by the Silesian Ridge and receiving detrital input from western insular highs and northeastern continental sources (Książkiewicz, 1956; Golonka et al., 2005, 2014; Ślączka et al., 2006).

Previous studies mapped and characterised these beds (Burtan, 1954, 1966a, b, 1978) and included ichnological (Uchman, 2008; Uchman and Szczęch, 2022) and micro-/macropalaeontological analyses (Vašíček et al., 2010; Kędzierski and Ochabska, 2012). The exposures, 0.5–4 m high on both banks of the river, show beds dipping northwest at angles between 52 and 84°. The southern section is relatively undisturbed (for a distance of ~200 m), whereas the central and northern parts show tectonic deformation (faults, folds, thrusts). The section belongs to the Beskid Mały Silesian series, Lanckorona facies (Książkiewicz, 1951). The Upper Cieszyn and Hradište Beds (Valanginian–Hauterivian) are overlain by the Veřovice Formation (upper Hauterivian–lower Albian; Fig. 2), tectonically reduced in the Krzyworzeka river section.

The succession mainly consists of very thin-bedded calcareous turbidites with hemipelagic caps, representing a distal, low-energy depositional system. Bed thickness and sedimentary characteristics are relatively uniform throughout the section. Distinct rusty beds indicate geochemical variations; coarse-grained sandstones and conglomerates appear in lenses. The upper part of the section comprises medium-bedded

sandstones that differ in character from the dominant very thin-bedded turbidites and indicate a sediment source distinct from that of the coarse-grained sandstones and conglomerates exposed in lenticular bodies.

AGE OF THE SUCCESSION

The Krzyworzeka section lacks precise dating, introducing potential uncertainties for cyclicity analysis. Biostratigraphic data were revised to support depth-to-time conversion. Ammonites, including *Criosarasinella mandovi* and *Teschenites subflucticulus*, indicate the Furcillata Zone (latest Valanginian; Vašíček et al., 2010). Calcareous nannoplankton from the same sample indicated a late Hauterivian to late Barremian age, and dinoflagellates suggested a Hauterivian age (Vašíček et al., 2010). The Hauterivian GSSP has since been revised, shifting its base from 136.4 Ma to 132.6 Ma (Mutterlose et al., 2021), which placed the recognised nannoplankton and dinoflagellates also in the latest Valanginian (Harding, 1986; Bown et al., 1998), supporting an age of ~133 Myr for the northernmost part of the section.

From the overlying Veřovice Beds, the ammonites *Hamulina asteriana* and *Bochianites* (Kokoszyńska, 1949) indicate an age of 130–129 Myr (Sepkoski, 2002; Klein et al., 2007). This constrains the Upper Cieszyn and Hradište Beds to the Valanginian (the oldest deposits were never described as Berriasian, and are therefore younger than 137 Myr) and early Hauterivian (~137–130 Ma), rather than Valanginian–middle Barremian (Uchman and Szczęch, 2022; Uchman et al., 2023), reducing the deposition duration from 9.5 to 7 Myr.

The 440 m-thick succession of the Upper Cieszyn Beds and Hradište Beds (Fig. 2) spans between ~137 Myr (base of the Valanginian) and ~130 Myr (onset of the Veřovice Beds). The 220 m-thick interval examined here represents its lower part, with the top dated at ~133 Myr (Fig. 2). The basal Upper Cieszyn Beds, exposed 100 m upstream at Poznachowice Dolne, are currently unexposed at this locality, indicating that the succession studied (about half of the total sequence) was deposited over ~3 Myr (136–133 Ma), in the *Criosarasinella Furcillata* Tethyan ammonite Zone (Reboulet et al., 2018). While the biostratigraphy-based depositional timeframe estimation lacks high precision, the depth-to-time calculation is done for a 2.5–3.5 Myr interval, with the highest probability of a 3 Myr depositional timeframe.

METHODS

Recent advances in numerical techniques have enabled detailed analyses of interactions between orbital forcing and sedimentary processes. Conventionally, Fourier transform-derived univariate time series analysis methods have been relied on in cyclostratigraphy (e.g., Hinnov, 2000; Weedon, 2003; Hilgen et al., 2014; Kodama and Hinnov, 2015). Several lesser-known approaches include autocorrelation, autoassociation, recurrence plots (RPs), and singular spectrum analysis (SSA), and these address limitations of Fourier transform-based methods, allowing for the detection of cyclicity even in noisy or short datasets. In Earth sciences, multivariate time series analysis has gained widespread use across, e.g., geophysics and climatology, but remains virtually absent from cyclostratigraphic studies.

As a first step, this study applies an integrated set of numerical techniques to verify whether the facies data series is random, influenced by deterministic processes, or exhibits a cyclic pattern. Subsequently, autoassociation, recurrence plots, and multi-channel singular spectrum analysis (MSSA) are employed to identify dominant cyclicities across all facies recognized.

A lithological log was created for both riverbanks, measuring all exposed Lower Cretaceous deposits at millimetre resolution. For statistical analysis, only the left-bank log was used due to minimal disturbance (Fig. 2A). Beds were traced over km-long distances, with lithology, internal structures, bioturbation, sole marks, grain size, and colour described, with special attention paid to tectonic deformation structures. Rock samples were collected, cut, and seventeen thin sections were prepared. Based on these observations, five main facies were distinguished (Appendix 1B1). The measured thicknesses of the facies sequences were treated as a 1 mm interval time series. The focus was on the cyclicity of enhanced clastic input (thicker sandstones and conglomerates) and oxidation variations (rusty beds), not individual turbidites. The left-bank log analysed totals 219.996 m, with each millimetre assigned a facies (Supplement A). To improve computational efficiency, binary-coded facies presence/absence data were resampled at 10 cm intervals. Comparison of smoothed charts at 1 mm and 10 cm resolution showed minimal differences, thereby supporting the use of 10 cm intervals for all numerical analyses. Statistical analyses, autoassociation, and recurrence plots were carried out based on presence/absence data series representing individual facies. For the multi-channel singular spectrum analysis, all facies occurrence data series were jointly regarded as a multivariate binary time series consisting of five channels, each with N = 2199 binary data points. Prior to the analysis, data gaps from seven unexposed intervals (2.21–2.51, 3.91–4.11, 88.91–92.51, 113.91–116.11, 177.61–179.51, 181.91–184.81, and 211.21–212.91 m) were replaced with zeros.

STATISTICAL ANALYSES

The runs test (Davis, 2002) was applied using PAST software (Hammer et al., 2001) to assess whether the dataset is completely random. It tests the null hypothesis of total randomness and independence between variables (Longhitano and Nemec, 2005; Hammer and Harper, 2024). The total number of runs for each facies separately, U, was compared to critical values at = 0.05. The Hurst statistic (K), used to assess clustering of thicknesses (n = 731), was calculated in OriginLab with the R/S method algorithm of Weron (2002).

AUTOASSOCIATION

Autoassociation, the binary-data counterpart of autocorrelation, detects characteristic patterns and possible cyclicity in time series (Hammer and Harper, 2024). It was applied to the nominal data of the beds corresponding to each facies occurrence. It enabled a comparison of a time series with delayed versions of itself (Davis, 2002). The autoassociation was treated as an introductory, exploratory method; no statistical significance was assessed. Results are shown in an autocorrelogram, plotting the correlation coefficient versus time lag, where higher peaks indicate cyclicity. Completely random, independent data will show low autoassociation values (except at lag = 0). Lags exceeding $^1/_4$ of the total series length were truncated, so the autocorrelogram presented covers lags of less than 50 m. Analysis was performed using PAST software (Hammer et al., 2001).

MIDPOINT-TRIANGLE INTERPOLATION AND SPECTRAL ANALYSIS

Facies thickness data were subjected to midpoint-triangle interpolation (Yao and Hinnov, 2019), enabling analysis of unevenly spaced data by transforming it to an evenly spaced series. This involved calculating the midpoint of each continuous occurrence of a given facies.

As facies F1 is dominant in the whole section, it was treated as a background facies for the other facies that appear cyclically. Unexposed intervals are most likely constituted of facies F1 and were also treated as background facies. Facies F5 was also treated as a background facies, as it only appears in the upper part of the section, so it cannot be confidently analysed in the whole section. Subsequently, an ordering approach was employed, assigning ranks as follows: 0 for background facies F1, facies F5, and unexposed intervals; 1 for facies F2; 2 for facies F3; and 3 for facies F4, thereby generating a "boxcar" series, allowing simultaneous analysis of all facies. Linear interpolation at 0.01 m intervals in Acycle (Li et al., 2019) produced a "triangle" series with smoother transitions and fewer discontinuities.

The interpolated time series was linearly detrended to avoid biasing low-frequency spectral components (Weedon, 2003) and analysed using the Lomb-Scargle algorithm (Press et al., 1993) with the rigorous smoothed window averages (SWA) spectral background estimation (Weedon et al., 2019; Weedon, 2022) in Acycle. This approach identified significant spectral peaks, including those exceeding the 5% false detection rate (FDR).

RECURRENCE PLOTS

Recurrence plots (RPs) visualise complex system dynamics and have recently been introduced to geological studies of ancient climate records (Marwan et al., 2021) and biotic dynamics (Spiridonov, 2017). While recently used in Jurassic sedimentary time series (Ninard et al., 2024), RPs have not yet been applied to turbiditic sequences. Here, RPs were used to assess applicability for geological time series and to analyse cyclicity of facies not detectable by other methods. It allows the assessment of time-series stationarity, which in cyclostratigraphy is commonly investigated using wavelet analysis or evolutionary spectral analysis. These approaches were also applied here (Appendix 1C) and produce broadly consistent results. Nevertheless, recurrence plots provide a more intuitive and robust visualization of changes in stationarity and cyclicity, particularly in noisy and highly non-stationary records such as those typical of unstable turbiditic successions. RPs visualise a square matrix where each element represents the time period during which a specific state of a dynamic system is observed. The recurrence plot displays all the time periods in which the trajectory of the system's phase space occupies the same region in phase space (Marwan et al., 2007). Natural processes can exhibit various recurrence behaviours, such as cyclical (e.g., seasonal or Milankovitch cycles) or irregular (e.g., El Niño), which are visualised in the recurrence plots. Different typologies and textures can be identified on these plots (Appendix 1B3), including (1) homogeneous (uniformly distributed noise), (2) periodic (superimposed harmonic oscillations), (3) drift (a logistic map corrupted by a linearly increasing term), and (4) disrupted (which in geological context may reflect abrupt transitions of environmental conditions; Marwan et al., 2021). Textures on a smaller scale feature isolated dots, and diagonal or horizontal/vertical lines. Isolated dots appear only where states are rare or highly variable. Diagonal lines indicate regions where the trajectory remains parallel to another segment (i.e., the system is in the same region of phase space at different times). The length of the diagonal line corresponds to the duration of similar evolution in the segment, while its distance from the main diagonal (the symmetry axis) represents the cyclic pattern of facies repeatability period. For geological data, the length of the diagonal lines indicates sections of the log where cyclicity can be detected, while the distance from the main diagonal denotes the cycle length in those sections (Marwan et al., 2007).

The recurrence analysis was performed on data expressed in metres, allowing for the identification of cycle lengths and the detection of log segments where cyclicity is observable. This was conducted on facies occurrence data: one analysis focused on detecting the cyclic pattern of facies F1–F5 repeatability, using a hybrid approach combining raw binary data with an equivalent smoothed variant of the same data, which was adopted after Ninard et al. (2024). The smoothing spline algorithm (De Boor, 2001) in PAST software (Hammer et al., 2001) was used to conduct locally weighted estimation of the density of "1s" in binary data series. Raw binary and smoothed counterpart data were juxtaposed using an interdependent neighbours recurrence criterion implemented in the Cross Recurrence Plot Toolbox (Marwan et al., 2007) in MATLAB software. The estimation of optimal delay and embedding dimension was performed via time-delayed mutual information quantification and false nearest neighbours statistics. Thresholds were set as low as possible for clear, readable plots (Marwan, 2011).

MULTI-CHANNEL SINGULAR SPECTRUM ANALYSIS

Spectral estimation was performed using multi-channel singular spectrum analysis (MSSA) to obtain an integrated representation of cyclicity across all facies distinguished. As the deposition of the different facies in fact did not occur independently, applying a multivariate time-series analysis method allows detection of the cyclicity in one measured multivariate time series, instead of comparing the cyclicity of each facies separately. MSSA is a multivariate extension of singular spectrum analysis (SSA) applicable to both continuous and binary data. This approach combines information from all channels (*sensu* variables) while preserving channel-specific variability (Zhang et al., 2018). As a non-parametric method, MSSA requires no assumptions regarding time-series stationarity or ergodicity (Alessio, 2016). Raw binary (presence/absence) time series with 0.1 m sampling interval for each of the five facies were used without further pre-processing. MSSA was conducted using kSpectra 3.9 software (Ghil et al., 2002) with a reduced covariance matrix. The window length was set to 1099 (N/2), providing maximum spectral resolution, and the sampling step to 0.1 m, allowing interpretation of the resultant spectrum in cycles per metre. To validate the robustness of the results, MSSA was repeated multiple times with a range of smaller window lengths (Alessio, 2016). This procedure resulted in a very similar spectral pattern, albeit with lower spectral resolution.

The significance of dominant cyclic components against the spectral background was assessed at the = 0.05 level using a Monte Carlo approach (Weedon, 2003), with 500 Monte Carlo surrogate series derived from the AR(1) process. Owing to the bilateral nature of the test, error bars spanning 2.5th to 97.5th percentiles of the noise distribution were generated in kSpectra. To be consistent with a standard cyclostratigraphic practice of plotting one-sided confidence levels (CL), upper limits of the error bars were converted to 97.5% CL (Weedon, 2003; Alessio, 2016). Spectral peaks exceeding this CL are statistically distinct from the red-noise spectral background at 97.5% confidence.

Fig. 3. Representative photographs of the main sedimentary facies distinguished in the Krzyworzeka river section: F1 (A), F2 (B, C), F3 (D), F4 (E), and F4 (F)

SENSITIVITY ANALYSIS OF ALTERNATIVE FREQUENCY-TIME INTERPRETATIONS

To assess the robustness of cycle duration interpretation against the uncertainty of the total depositional timeframe model, a sensitivity analysis was conducted. The best estimate of the depositional timeframe is 3 ±1 Myr (see section 2.2). Five discrete depositional timeframe variants covering the full extent of the parameter space were analysed: a 3 Myr baseline and four alternatives (2 Myr, 2.5 Myr, 3.5 Myr, and 4 Myr). For each cycle wavelength determined, corresponding time domain cycle durations were calculated as proportions under each of the five timeframe variants. The distribution of interpreted cycle durations was visualized using MATLAB-generated plots, with individual variants overlaid to illustrate the proportional scaling of temporal uncertainty relative to cycle wavelength.

RESULTS

In the 220 m section studied, five facies (F1–F5) were distinguished, constituting one depth series, in which one facies follows another, as well as five separate depth series for each facies for MSSA (Appendix 1A, B1). Facies F1 dominates (Fig. 3A) and consists of calcareous turbiditic mudstones interbedded with very thin-bedded, fine-grained, and very fine-grained calcareous sandstones, usually capped by a very thin, hemipelagic mudstone. This is comparable to facies C2.3 of Pickering et al. (1986), but with higher mudstone-to-sandstone ratios and no fining-upwards trend. Mudstones are massive, dark grey, 5–150 mm thick (rarely up to 470 mm), while the sandstone beds vary between light grey and dark grey, with thicknesses typically ranging from 1 to 30 mm (rarely up to 90 mm). The mudstones are bioturbated (30–50%) with the common ichnofossil *Chondrites*, and may contain ammonites, aptychi, and belemnites. The bases of the sandstones are sharp and erosive, and they gradually change into mudstones towards the top. Both parallel and cross laminations (Tb–Tc intervals of the Bouma sequence) and thin mudstone laminae are commonly present in the sandstones. The facies F1 deposits are continuous for up to 20 m and interbedded with facies F2, F3, F4, and F5 deposits.

Facies F2 (Fig. 3C, D) is distinguished by its rusty colour and consists of sideritic mudstones, siltstones, and sandstones. The sideritic beds are laterally extensive, not appearing in

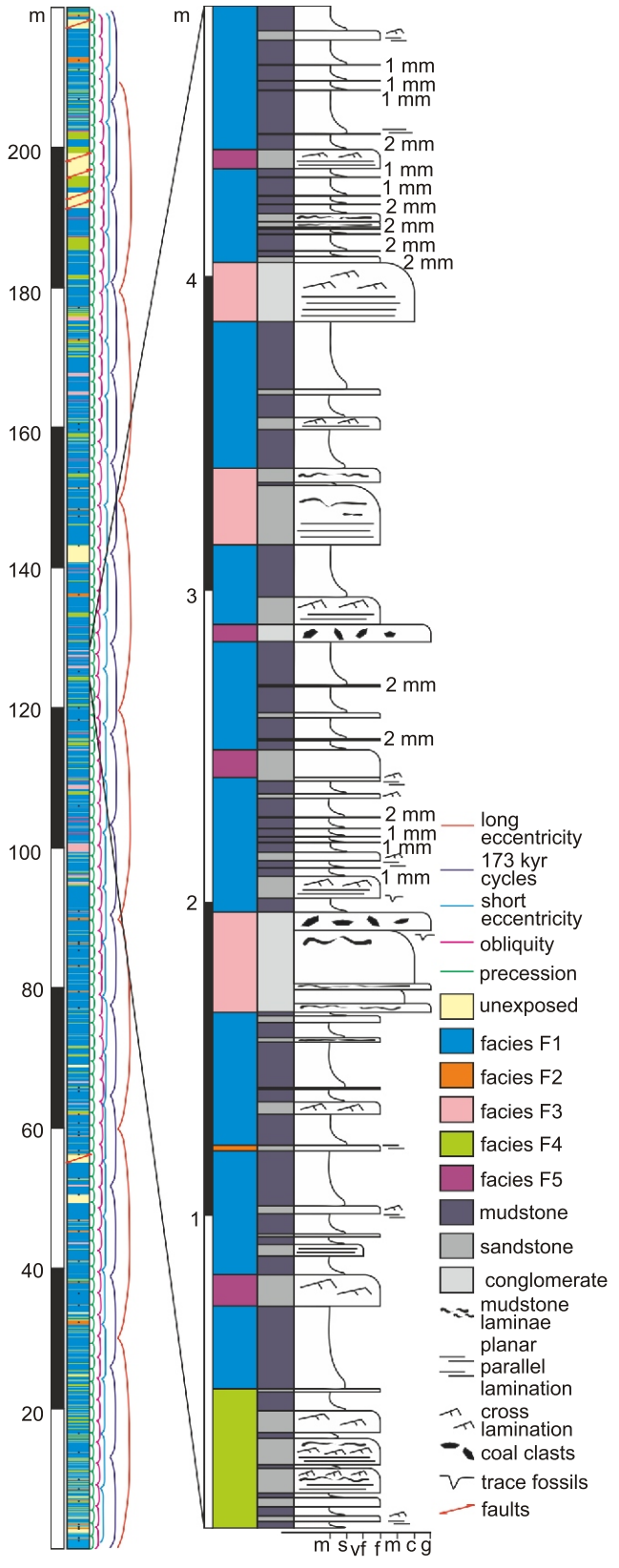

Fig. 4. Measured log with all of the distinguished facies and detected orbital cycles marked (the cycles are indicated schematically to illustrate their approximate number within the section, rather than their exact temporal positions)

3 Myr depositional time assumed. Facies F2 beds are marked with a black dot. A representative sedimentological log is shown on the right

lenses; the rusty colour usually appears on the rock surface, along some laminae, and in the fracture infills. Sideritisation is occasionally observed in conglomerates and coarse-grained sandstones (Fig. 3D). Thin mudstone laminae are commonly found within the sandstone beds. The facies F2 beds are typically 1–30 cm thick, and occasionally facies F2 appear as couplets of sideritic beds and dark grey, thin mudstone beds up to 75 cm thick. Most of the sideritic sandstones are of turbiditic origin; however, some environmentally induced factors led to their distinctive sideritic appearance. One of the explanations is that periodic water freshening occurred, which influenced the reducing conditions. This is supported by the pyrite concentration occurring in the rusty laminae. The changes in colouration are unlikely to be the result of later diagenetic processes.

Facies F3 (Fig. 3E) consists of sandstones and conglomerates in concave-plane, asymmetrical lensoidal beds with a maximum thickness of up to 110 cm, interpreted as meandering channel infills. Locally, these lenses consist of amalgamated beds. The clasts in the conglomerates range from 2 to 80 mm in diameter and include quartz grains, limestones with sponges and corals (Štramberg-type facies), mudstones, lithic fragments, and occasionally coal. Mudstone intraclasts are also common. While the conglomerates are composed mostly of exotic clasts, they can be identified as facies F1.1 of Pickering et al. (1986). The sandstones are quartz arenites with a calcareous matrix (cf. Pickering et al., 1986 – B1.1). Usually, no lamination or other sedimentary structures occur within this facies.

Facies F4 (Fig. 3F) comprises predominant fine- and medium-grained sandstones, interbedded with mudstones, with a sandstone/mudstone ratio >1, sequences 3–40 cm thick (locally up to 170 cm), comparable to facies C2.3 of Pickering et al. (1986). Sandstones are thicker (10–50 mm), and locally coarser-grained than in facies F1 sandstones. The mudstone beds are typically 5–30 mm thick. This facies is reverse to the facies F1, where the mudstones are interbedded with thin sandstone beds. While F1 and F4 share similarities in sedimentary structures and mineralogy, they differ notably in their relative proportions of mudstone and sandstone, reflecting differences in terrigenous input intensity.

Facies F5 (Fig. 3B) includes laterally continuous medium-bedded sandstones and conglomerates (5–20 cm thick), fine- to medium-grained, with clasts up to 1 cm in diameter. Parallel and cross lamination are common, and a fining upwards trend, and coal clasts occur sporadically. The B2.1 facies of Pickering et al. (1986) describes these deposits best.

The 220 m-thick log is shown in Figure 4, alongside a representative sedimentological 'bed-by-bed' log. The average number of turbidites per metre in the studied log is 30.

The estimated Hurst statistic for the thicknesses data series is $K = 0.9$. A value close to 1, and well above the threshold of 0.5, indicates a strong tendency towards clustering (serial dependence), and a marked departure from randomness (Chen and Hiscott, 1999).

RUNS TEST

Binary-data runs tests (Appendix 1B2) revealed high Z values and $H0$ probabilities near 0 for all facies, allowing rejection of the null hypothesis. This confirms that occurrences of F1, F2, F3, F4, and F5 beds are non-random at 95% confidence.

AUTOASSOCIATION

The results of the autoassociation are shown in the autocorrelogram (Fig. 5). The autoassociation analysis suggests that a cyclic pattern of facies occurrence occurs in the section studied at intervals of 3.30 m, 4.65–6.13 m, 8.5 m, 12.2 m, 13.7 m, 19 m, 29.3 m, and 37.9 m (Table 1).

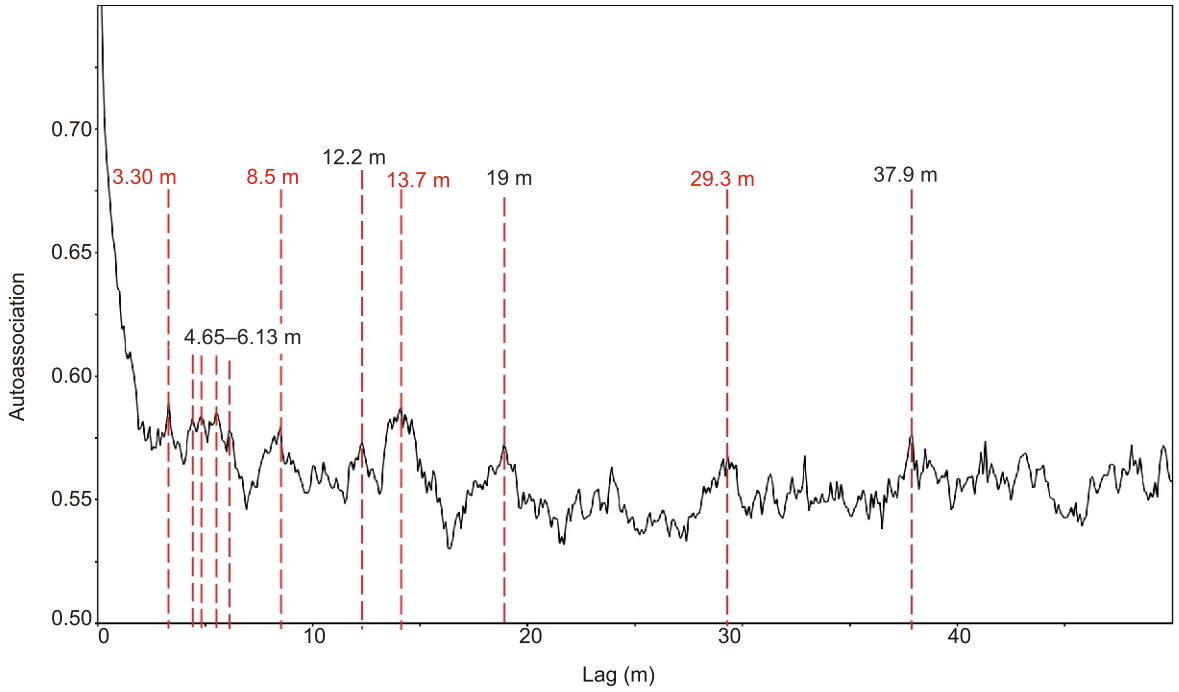

Fig. 5. Autocorrelogram from autoassociation analysis of the depth-series from the Krzyworzeka section

Prominent peaks are marked with red lines and indicate repeatability at specific depth intervals. Red-coloured cycle lengths correspond to periodicities that can be interpreted as orbital cycles, after depth-to-time conversion assuming a 3 Myr depositional timeframe. Lag (delay) units on the x-axis (1 lag unit = 1 m), autoassociation dimensionless units on the y-axis

Table 1

Cyclicities detected by autoassociation analysis of the dataset studied with their depth-to-time transitions, when a 3 Myr depositional timeframe is assumed

Period	Time (assuming 3 Myr depositional timeframe)	Interpretation
3.3 m	45 kyr	Obliquity
4.7–6.1 m	64.2–83.4 kyr	Autocyclicity or other non-orbital signal
8.5 m	115.9 kyr	Short eccentricity
12.2 m	166.4 kyr	Obliquity modulation
13.7 m	186.8 kyr	Obliquity modulation
19 m	259.1 kyr	Harmonic frequency (1/2 > 500 kyr cycle), autocyclicity, or other non-orbital cycle
29.3 m	399.5 kyr	Long eccentricity
37.9 m	516.8 kyr	Autocyclicity or other non-orbital cycle. Too few repetitions in the log to interpret

The interpretation column indicates possible links to orbital forcing or alternative mechanisms

MIDPOINT-TRIANGLE INTERPOLATION AND SPECTRAL ANALYSIS

Lomb-Scargle analysis with SWA confidence levels (Fig. 6) shows four peaks above 99% SWA confidence level (0.64, 0.36, 0.2, and 0.15 cycles/m), with two also exceeding 5% FDR (0.64 and 0.2 cycles/m), corresponding to repeatability periods of 1.57 m, 2.78 m, 5.1 m and 6.65 m (Table 2). The spectrogram was truncated at a minimum frequency of 0.025 cycles/m (frequencies lower than this would be excessively low for such a short data series; 0.025 corresponds to a 40 m repeatability period) and a maximum frequency of 1 cycle/m (as some facies occur significantly less frequently than every 1 m; truncation enhances spectrogram readability).

RECURRENCE PLOTS (RPS)

Recurrence plots (Fig. 7 and Appendix 1C) are symmetrical, with x- and y-values representing log length. Diagonal segments parallel to the symmetry axis indicate a cyclic pattern of facies repeatability within the log (Marwan et al., 2007). Coloured lines were drawn at locations where more than one diagonal segment occurred at a certain distance from the axis of symmetry (that means that cyclicity is detectable not only in one segment of the section, but in at least two longer segments). The distance from the symmetry axis corresponds to the cycle period.

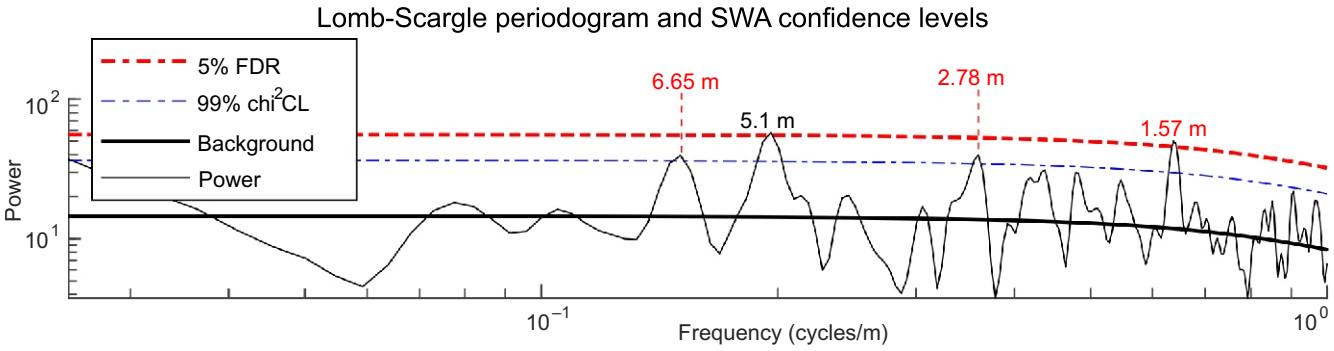

Fig. 6. Lomb-Scargle periodogram of midpoint-triangle interpolated data from the record studied. 99% chi^2 confidence levels and 5% false detection rate (FDR) marked

Peaks that could be assigned to orbital cycles are marked in red. Wavelengths in metres are shown above the respective peaks

Table 2

Cyclicities detected by spectral analysis of the record studied with their depth-to-time transitions, when a 3 Myr depositional timeframe is assumed

Period	Time (assuming a 3 Myr depositional timeframe)	Interpretation
1.6 m	21.9 kyr	Precession
2.8 m	38.3 kyr	Obliquity
5.1 m	69.7 kyr	Autocyclicity, or other non-orbital cycle
6.7 m	91.6 kyr	Short eccentricity

The interpretation column indicates possible correspondence to orbital forcing or non-orbital processes

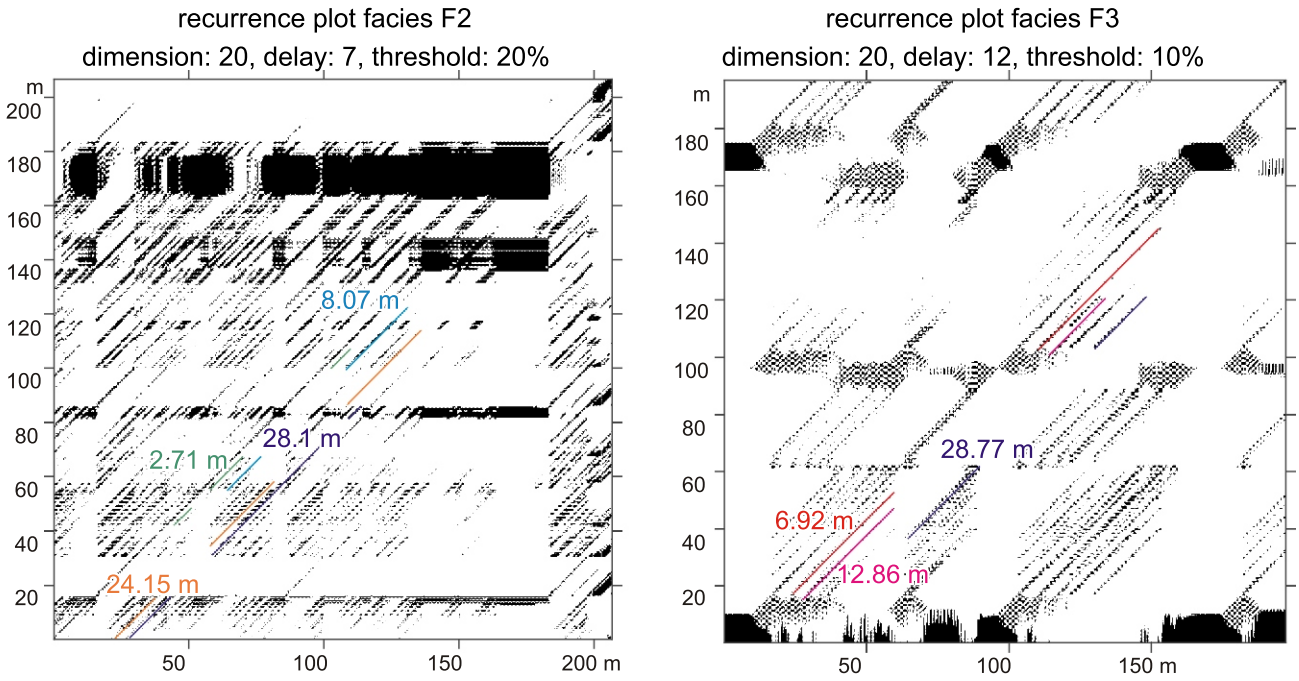

Fig. 7. Recurrence plots showing the repeatability of facies F2 and F3 from binary presence/absence series

Arrangements of diagonal lines corresponding to particular cycle wavelengths are marked with colours

Table 3

Cyclicities detected by recurrence plots analysis of the record studied with their depth-to-time transitions, when a 3 Myr depositional timeframe is assumed

Period	Time (assuming a 3 Myr depositional timeframe)	Interpretation
2.7 m (F2)	36.9 kyr	Obliquity
6.9 m (F3)	94.1 kyr	Short eccentricity
8 m (F2)	109.1 kyr	Short eccentricity
12.9 m (F3)	175.9 kyr	Obliquity modulation
24.2 m (F2)	330 kyr	Harmonic frequency (1/2 > 600 kyr cycle), autocyclicity, or other non-orbital cycle
28.1 m (F2)	383.2 kyr	Long eccentricity
28.77 m (F3)	392.3 kyr	Long eccentricity

Labels F2 and F3 denote recurrence intervals calculated for facies F2 and F3. The interpreted periodicities are compared with the expected orbital cycles

For F2, cyclicity occurs at intervals of 2.71 m, 8.07 m, 24.15 m, and 28.1 m (Fig. 7 and Table 3). In the recurrence plot for facies F3, cyclicity is observed at 6.92 m, 12.86 m, and 28.77 m (Fig. 7 and Table 3). Diagonal segments beyond these intervals are not considered in the analysis for reasons of reliability (cycles of lower frequency than every 35 m cannot be confidentially interpreted as cyclical in a 220 m thick log; Davis, 2002). The recurrence plots for facies F1, F4, and F5 showed no significant cyclicities, which are continuous in different parts of the log (Appendix 1C). The chaotic appearance may be the result of very frequent occurrences of facies F1 and F4, and the clustered appearance of facies F5.

MULTI-CHANNEL SINGULAR SPECTRUM ANALYSIS (MSSA)

MSSA revealed the cyclic pattern of facies occurrence in the section studied at intervals of 1.7 m, 4.8 m, 7.1 m, 12.5 m, and 16.7 m. (Fig. 8 and Table 4).

SENSITIVITY ANALYSIS OF ALTERNATIVE CYCLE DURATION INTERPRETATIONS

The sensitivity analysis demonstrates a linear dependence between the depositional timeframe model and the calculated cycle durations. As the deposition duration parameter varies from 2 to 4 Myr, representing the ±33% uncertainty bounds, the absolute magnitude of temporal uncertainty scales upwards with cycle wavelength (Fig. 9). For the shortest wavelengths, the impact of model uncertainty is relatively limited. For example, the 1.7 m cycles, interpreted as precession in the baseline model, range from 15.5 kyr to 30.9 kyr across the full parameter space. Conversely, low frequency cycles show significant absolute divergence. In the most extreme case, 28.7 m cycles – interpreted as long eccentricity in the baseline model – range from 261 kyr (in the 2 Myr variant) to 522 kyr (in the 4 Myr variant). Therefore, the time-domain conversion of eccentricity and obliquity modulation cycles is highly sensitive to the initial constraints of the depositional model (Fig. 9), allowing for robust orbital interpretation only when assuming minor discrepancies from the 3 Myr model.

DISCUSSION

The deep-marine succession studied exhibits clear periodicities in depositional events, such as increased terrigenous supply (facies F3–F5) and sideritic beds (facies F2). Periodicities identified through three independent methods can be grouped into distinct cycles of ~1.7, ~2.8, ~5.2, ~7.4, ~13, ~17.9, ~24.2 and ~28.7 m (Table 5). The cycles > 35 m were excluded because they occur too few times within the 220 m log to be evaluated reliably, as were cycles <1 m, which fall below the effective logging resolution and therefore cannot be interpreted with confidence. Orbital and harmonic cycles were distinguished by comparing detected periodicities to known Milankovitch frequencies (cf. Meyers et al., 2012; Zeeden et al., 2023; Li et al., 2024) and considering potential autocyclic or tectonic influences.

The depositional timeframe was determined using biostratigraphical data rather than sedimentation rates derived from hemipelagic intervals, which averaged out the inherent variability of turbidite systems. As a result, the reported values repre-

Table 4

Cyclicities detected by multi-channel singular spectrum analysis of the dataset studied with their corresponding periods in the time domain, when a 3 Myr depositional timeframe is assumed

Period	Time (assuming a 3 Myr depositional timeframe)	Interpretation
0.6 m	8.2 kyr	Confident interpretation not viable in the light of logging resolution and age model
1.7 m	23.2 kyr	Precession
4.8 m	65.5 kyr	Autocyclicity or other non-orbital signal
7.1 m	96.8 kyr	Short eccentricity
12.5 m	170.5 kyr	Obliquity modulation
16.7 m	227.7 kyr	Harmonic frequency (1/2 > 500 kyr cycle), autocyclicity, or other non-orbital cycle

The interpretation column presents possible links to orbital forcing or alternative mechanisms

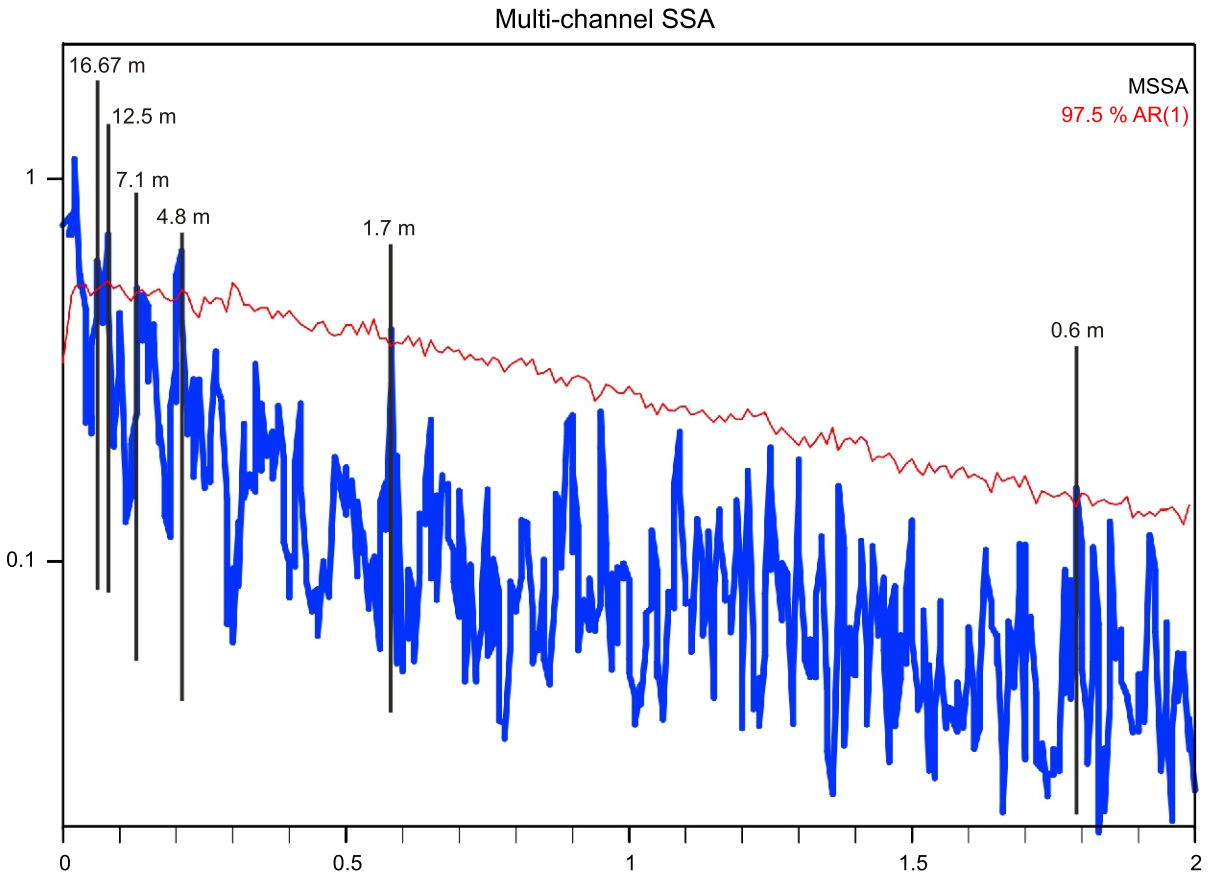

Fig. 8. Multi-channel singular spectrum analysis of multivariate facies presence/absence data series

Wavelengths (in metres) are indicated over peaks that are statistically significant relative to the AR(1) red-noise spectral background at a confidence level exceeding 97.5%

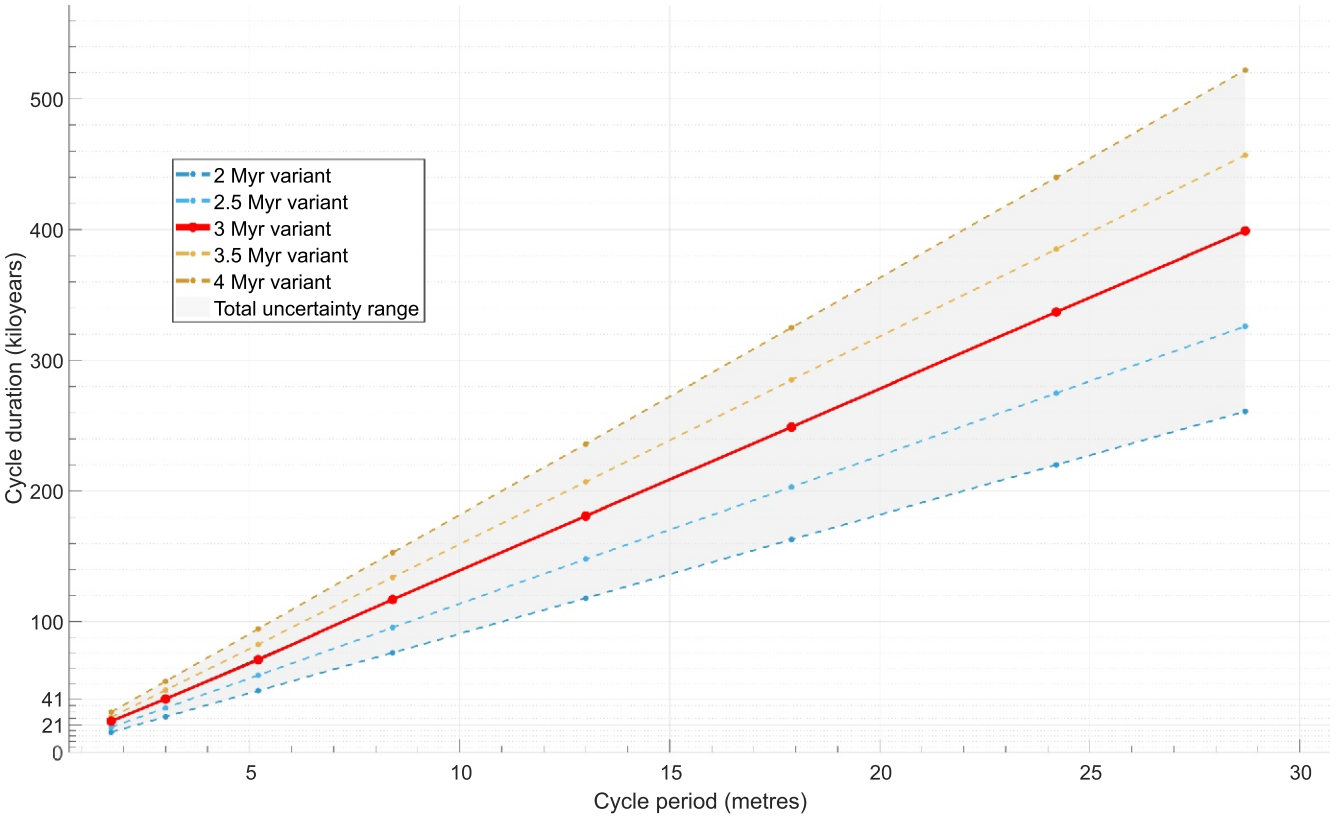

Fig. 9. Line plot of sensitivity analysis of depth-to-time conversion for assumed total depositional timeframe variants, relative to the 3 Myr baseline model

Intermediate variants and bounding 2 Myr and 4 Myr variants over a shaded uncertainty envelope show the divergence magnitude relative to cycle wavelength

Table 5

Cyclicities detected by all the methods applied with their depth-to-time transitions; 3 Myr depositional timeframe

Period (m)	Time (kyr)	Method	Cycle assigned
1.7 ± 0.1	23.9 ± 1.4	Lomb-Scargle transform; MSSA	Precession
2.8 ± 0.1	38.3 ± 1.4	Autoassociation; Lomb-Scargle transform; RP F2	Obliquity
5.2 ± 0.9	70.9 ± 12.3	Autoassociation; Lomb-Scargle transform; MSSA	Autocyclicity or other non-orbital cycle
7.4 ± 1.1	101.1 ± 15	Autoassociation; Lomb-Scargle transform; RP F2; F3 MSSA	Short eccentricity
13 ± 0.7	180.8 ± 9.7	Autoassociation; RP F3; MSSA	Obliquity modulation
17.9 ± 1.1	248.7 ± 15.3	Autoassociation; MSSA	Autocyclicity or other non-orbital cycle
24.2	336.6	RP F2	Autocyclicity or other non-orbital cycle
28.7 ± 0.6	399.2 ± 9.2	Autoassociation; RP F2, F3	Long eccentricity

For each cycle, the table reports median period values with associated uncertainties, based on ranges identified by different methods. The assignment of cycles to orbital or non-orbital origins is indicated

sent an average depositional rate for the entire succession; however, a constant sedimentation rate is not assumed. The analysis emphasizes facies cyclicity rather than frequency of individual turbidites, with thin-bedded turbidites and mudstones grouped into a single facies (F1). This approach ensures that variations in the recurrence of individual turbidite beds do not influence the broader temporal framework.

As the section studied lacks precise age-dating, the depth-to-time conversion may be subject to debate. The base of the 440 m-thick Upper Cieszyn and Hradište Beds is likely lowermost Valanginian (~137 Ma; Geroch, 1966; Szymakowska, 1981; Szydło, 1996; Uchman, 2004; Ślączka et al., 2006; Vašíček et al., 2010; Mutterlose et al., 2021), while its top is ~130 Ma (Szymakowska, 1981), implying deposition over ~7 Myr, with the 220 m Krzyworzeka section representing <3.5 Myr. Assuming a 3 Myr depositional timeframe (~136–133 Ma, as explained in Section 2.2), the Lower Cretaceous deep-marine turbiditic cycles show a strong correlation with precession, obliquity, short eccentricity, long eccentricity, and 173 kyr obliquity modulation. As the depositional timeframe in the section studied may be subject to debate, the interpretation of prominent peaks under different sedimentation rates is provided (Table 6). While assuming depositional timeframes of 2, 2.5, 3.5, or 4 Myr, some periodicities may accidentally match orbital frequencies. However, assuming the 3 Myr timeframe allows the detection of both short and long eccentricity, as well as

Table 6

Variant depth-to-time cyclicities conversion (with uncertainties) assuming four alternative depositional timeframes: 2, 2.5, 3.5 and 4 Myr

Period (m)	2 Myr (1 e./300 y)	2.5 Myr (1e./400 y)	3.5 Myr (1 e./600 y)	4 Myr (1 e./ 660 y)
1.7 ± 0.1	15.5 kyr ± 0.9	19.3 ± 1.1 kyr (precession)	27 ± 1.6 kyr (precession)	30.9 ± 1.8 kyr
2.8 ± 0.1	25.5 ± 0.9 kyr (precession)	31.8 ± 1.1 kyr	44.5 ± 1.6 kyr (obliquity)	50.9 ± 1.8 kyr
5.2 ± 0.9	47.3 ± 8.2 kyr (obliquity)	59.1 ± 10.2 kyr	82.7 ± 14.3 kyr (short eccentricity)	94.5 ± 16.4 kyr (short eccentricity)
7.4 ± 1.1	67.5 ± 10 kyr	84 ± 12.5 kyr (short eccentricity)	117.5 ± 17.5 kyr (short eccentricity)	134.5± 20 kyr
13 ± 0.7	118.2 ± 6.4 kyr (short eccentricity)	147.7 ± 8 kyr	206.8 ± 11.1 kyr	236.4 ± 12.7 kyr
17.9 ± 1.1	162.7 ± 10 kyr (obliquity modulation)	203.3 ± 12.5 kyr	284.8 ± 17.5 kyr	325.4 ± 20 kyr
24.2	220 kyr	275 kyr	385 kyr	440 kyr
28.7 ± 0.6	260.9 ± 5.5 kyr	326.1 kyr	456.6 ± 9.5 kyr	521.8 ± 10.9 kyr

The resulting time periods are colour-coded according to their interpreted astronomical origin: green = precession, yellow = obliquity, red = short eccentricity, grey = obliquity modulation. E. = turbiditic event, the turbiditic event frequency (1 event per X years) is indicated for each depositional timeframe

precession, obliquity, and obliquity modulation cycles, and fits best into regional stratigraphical interpretations. A shorter depositional timeframe would imply extremely high turbidite frequency (e.g., 1 event/300 years), and a longer depositional timeframe does not correspond well with known stratigraphic data. Thus, 3 Myr is considered an approximate depositional timeframe. It is not possible to estimate it with greater accuracy; however, assuming a depositional timeframe in the range of 2.5–3.5 Myr, the interpretation does not change radically, and the periodicities match the same orbital cycles (Fig. 9 and Table 6). The sensitivity analysis results indicate that higher frequency cycles are less sensitive to depositional timeframe change, while low frequency cycles are more sensitive. That is why the detection of low-frequency cycles, especially long eccentricity and obliquity modulation, is more sensitive to depositional timeframe uncertainties, while the precession and obliquity influence can be established with greater confidence, assuming a 2.5–3.5 Myr depositional timeframe. The 3 Myr variant induces a ~73 m/Myr sedimentation rate, which is reasonable compared with estimates of other Alpine system Valanginian sections (20–70 m/Myr; e.g., Giraud et al., 1995; Egger and Schwerd, 2007; Charbonnier et al., 2013). Additionally, a TimeOpt analysis (Meyers, 2015) was performed to statistically assess sedimentation rates (Appendix 1E), and yielded estimates consistent with biostratigraphic constraints. However, the application of TimeOpt requires a relatively constant sedimentation rate at the scale of the section studied, an assumption that is generally valid for pelagic or hemipelagic deposits. In contrast, turbiditic systems are characterized by highly episodic sedimentation, where deposition occurs during gravity-flow events separated by variable periods of non-deposition. The time intervals between individual turbidite events may vary substantially. Such event-driven and irregular accumulation violates the assumption of quasi-continuous sedimentation required for TimeOpt, making its application to this dataset problematic.

Autoassociation detected (Table 1 and Fig. 5) the following cycles: the distinct obliquity modulation cycle (166.4 kyr and 186.8 kyr; 12.2 m and 13.7 m), the long eccentricity (399.5 kyr; 29.3 m) cycle, the short eccentricity (115.9 kyr; 8.5 m), and obliquity (45 kyr; 3.3 m), but it failed to identify precession. Spectral analysis provided on midpoint-triangle interpolated data detected (Table 2) precession (21.9 kyr, ~1.6 m), obliquity (38.3 kyr, ~2.8 m), and short eccentricity (91.6 kyr, ~6.7 m). RPs (Table 3) revealed the long eccentricity (392 kyr, ~28 m), short eccentricity (94 kyr, ~7 m), and obliquity modulation (172 kyr, ~13 m) cycles for facies F3 and the long eccentricity (383 kyr, ~28 m), short eccentricity (110 kyr, ~8 m), and obliquity cycles (37 kyr, ~2.7 m) for facies F2. The precession cycle was detected only through MSSA (23 kyr, 1.7 m). The MSSA analysis also detected short eccentricity (96.8 kyr, 7.1 m) and obliquity modulation (170.5 kyr, 12.5 m), but failed to detect obliquity and long eccentricity (Table 4). In addition, there was also an 8.2 kyr (0.6 m) cycle detected in the MSSA analysis, which must be interpreted with caution; however, its length matches the sub-Milankovitch ~8 kyr cycle (e.g., Aziz et al., 2008; Boulila et al., 2010; Wu et al., 2012). The short eccentricity cycle was consistently detected across all methods, and RPs for facies F2 and F3 also revealed this signal. RPs and MSSA detected a periodicity which corresponds more with the ~95 kyr eccentricity component, whereas autoassociation aligned with the ~125 kyr eccentricity component. The obliquity modulation (~173 kyr) cycle was also detected by all methods except Lomb-Scargle spectral analysis; however, RP for F2 did not detect it. Therefore, short eccentricity appears to have exerted the strongest control on the sedimentation of the deposits studied.

Several periodicities remain unassigned to known orbital forcing (~70, ~249 and ~337 kyr). These may represent harmonics of longer, likely non-orbital cycles, or reflect autocyclicity or intermittent tectonic activity rather than climatic forcing. Future studies, including high-resolution core analyses, could help clarify their origin.

The cyclicity of facies reflects changes in erosion rates, with facies F1 deposited in distal settings under reduced terrigenous supply, and F3–F5 corresponding to increased sediment input, particularly coarse-grained beds. The increased sediment input may be related to increased continental runoff, caused by higher precipitation rates associated with orbitally-induced changes in insolation, as explained by Weltje and de Boer (1993). The occurrence of Štramberg-type limestone clasts in the conglomerates indicates that the material was partly transported from a carbonate platform. Redeposition from the carbonate platform, resulting in coarse-grained, medium-bedded facies, might have been more intense during sea-level fall, causing shelf edge instability and enhanced downslope transport of the material. The cyclic pattern of facies F2 beds is more complex. These deposits underwent sideritisation, which requires detailed geochemical investigation. The introductory geochemical analysis (SEM-EDS) indicates a synsedimentary origin of sideritization related to pyrite occurrences. Recent work by Mitchell et al. (2021) demonstrated that orbital forcing can influence the periodic oxidation of ferrous iron in banded iron formations. The periodicity of facies F2 appears to be primarily related to obliquity, as well as to short and long eccentricity (Table 3). If the deposition of sideritic beds was linked to oxidation or nutrient variations, obliquity may have played a significant role. The relationship between ferrous iron and orbital cycles requires further investigation in the context of deep-marine turbiditic environments. The influence of obliquity, and especially of the obliquity modulation on sedimentation, appears to be more pronounced in this study than in previous research. For example, Ten Kate and Sprenger (1993) found that eccentricity cycles dominated sedimentary processes, with obliquity having a lesser impact at low palaeolatitudes (20°N). The Proto-Silesian Basin's palaeolatitude during the Early Cretaceous (~35°N; Stampfli and Hochard, 2009) likely enhanced obliquity-driven climatic effects, such as seasonal temperature and precipitation contrasts, which influenced erosion rates and terrigenous sediment supply. Meyers et al. (2012) highlighted the role of obliquity cycles in modulating seasonal contrasts and their potential impact on deep-marine sedimentation through enhanced erosion and material supply. Importantly, orbitally paced monsoon-driven hydrological variability has been identified in Valanginian successions of the northwestern Tethys, where cyclic changes in detrital flux and sediment accumulation are linked to precession and eccentricity forcing (Charbonnier et al., 2016). A similar mechanism may therefore provide a plausible climatic framework for the cyclicity observed in the succession studied. Obliquity modulation cycles of 173 kyr seem to be more present in the sedimentary record studied than previously postulated elsewhere (e.g., Huang et al., 2021; Yao et al., 2022; Li et al., 2024; Pieńkowski et al., 2024).

Some of the cycles detected correspond to known orbital periodicities, whereas others may reflect tectonic repetitions or autocyclic processes inherent to turbidite systems. The high Hurst exponent (K = 0.9) indicates strong persistence, consistent with a dominant allocyclic influence. Field observations revealed no evidence of channel migration, channel–levee deposition, or other indicators of autocyclic control; nonetheless, such processes cannot be entirely excluded. For the channel-levee system, a massive channel facies succession would have been required, though none of these are described from

the Early Cretaceous in the study area or in the Proto-Silesian Basin. While the rhythmically bedded very thin turbidites could be potentially interpreted as levee facies, no channel has been found that would produce such an amount of levee deposits and be connected with the levee. Traction processes dominated the sedimentation in the succession studied, rather than suspension fallout. Likewise, detailed structural analysis during logging showed no signs of significant tectonic repetition. The results reveal cycles both consistent with and independent of orbital forcing, underscoring the complex interplay of controlling mechanisms in the turbidite system. Although autocyclic processes were undoubtedly present, orbital signals appear stronger than previously suggested. The detection of any orbital imprint in such a complex depositional setting is noteworthy, as deep-sea sedimentation is mediated by processes in shallower zones that are themselves modulated by orbital forcing, even if partially masked by autocyclic processes. Detecting such signals is generally more challenging in open and complex basins than in confined ones. The basin studied shows no evidence of confinement, yet orbital forcing was still detected, suggesting that such signals can be preserved even in spatially extensive systems. Turbidite systems, regardless of scale, commonly record variations in sediment supply and triggering mechanisms, expressed in changes in frequency, thickness, or grain size of beds. These patterns may reflect larger-scale cyclicity and are not necessarily restricted to basins with continuous turbidite coverage. While only one section was analysed in detail, the entire 220-m thick succession exposed on both sides of the Krzyworzeka river was logged, and no indicators of channel migration or other autocyclic factors were observed.

This study identified cyclicity through facies changes, as demonstrated by applying three independent methods. Autoassociation and MSSA enabled the detection of general sequence repeatability, while RP analyses focused on the cyclic pattern of specific facies occurrences. Recurrence plots and MSSA represent novel applications in the study of turbiditic sequences, with their effectiveness demonstrated in this study. Ninard et al. (2024) recently introduced recurrence plots in geological time series analysis, the present study being an extended application of the method in turbiditic environments. RPs and autoassociation appear to be more effective in detecting lower-frequency cycles, while MSSA and midpoint triangle interpolation Lomb-Scargle transform additionally showed sensitivity to higher-frequency cycles. Recurrence plots were also unsuccessful in detecting cyclicity in facies F1 and F4, which are much more frequent throughout the section compared to F2 and F3. Similarly, no cyclicity was identified for facies F5, which is restricted to the upper part of the section. These results suggest that recurrence plots may be more effective for detecting cyclicity in features that occur less frequently but consistently within a time series.

The integration of different methods for cyclicity analysis enables the detection of the most prominent cycles by comparing their expressions across various models rather than relying solely on peak size comparisons. This approach facilitated a comprehensive cyclicity analysis, overcoming challenges posed by interrupted time series and limited exposure. However, further research is necessary to validate these methods across different depositional environments and patterns of exposure. Recurrence plots and MSSA show considerable promise for future applications, especially in cases where traditional spectral analyses may lack sufficient sensitivity.

The frequency of turbidite events approximates one event every 454 years. This is a remarkably similar value to the one event every 487 years postulated by Uchman (2004), and corresponds with the frequence of recent turbidity currents recorded in Hawkes Bay, New Zealand (~1 event/400 years; e.g., Lewis and Kohn, 1973). This represents one of the highest frequencies recorded in the Outer Carpathians (Uchman, 2004). Even though the average frequency of turbiditic events is calculated, it is known that individual turbidite events may have occurred with various frequencies; a constant sedimentation rate is not assumed here. For this reason, the cyclicity of individual turbiditic events is not addressed in this study. More precise dating of the section – particularly at its base – would allow a more reliable conversion to time.

CONCLUSIONS

The deposits studied represent a distal turbidite lobe system, characterized by cyclically deposited coarser-grained and medium-bedded deposits, as well as cyclically occurring sideritization, which reflects orbitally modulated episodes of intensified terrigenous influx or water freshening, among the dominant, very thin-bedded fine-grained turbidites.

The cyclicities detected are mostly allocyclic, which is corroborated by the calculated Hurst exponent, as well as by detailed sedimentological investigation.

An integrated suite of exploratory and confirmatory numerical methods, including runs test, autoassociation, spectral analysis, recurrence plots, and multichannel SSA, enabled the identification of precession, obliquity, eccentricity, and obliquity-modulation signals in deep-sea turbiditic deposits (220 m thick, measured in an almost continuous section) of the Lower Cretaceous of the Outer Western Carpathians. This approach facilitated a thorough analysis of the cyclicity, overcoming challenges associated with interrupted time series and limited exposure. The identification of cyclic patterns, combined with a revision of previous biostratigraphic data, provided new insights into the stratigraphy of the deposits studied; however, better chronostratigraphic control should be provided in the future through improved bio- or magneto-stratigraphy. The research demonstrated an exceptionally high frequency of turbiditic depositional events, occurring approximately once every 500 years.

Acknowledgements. The helpful review by Christian Zeeden allowed to improve the manuscript. We thank Gert Jan Weltje for his valuable comments on an early version of this work. Norbert Marwan is appreciated for providing the CRP Toolbox.

DATA AVAILABILITY STATEMENT

All data generated or analysed during this study are available in the appendicies of this article.

FUNDING

The paper was supported by a grant from the Faculty of Geography and Geology under the Strategic Program Excellence Initiative at Jagiellonian University.

REFERENCES

Alessio, S.M., 2016. Singular spectrum analysis (SSA). In: Digital Signal Processing and Spectral Analysis for Scientists. Signals and Communication Technology: 537–571. Springer, Cham.

Aziz, H.A., Hilgen, F.J., van Luijk, G.M., Sluijs, A., Kraus, M.J., Pares, J.M., Gingerich, P.D., 2008. Astronomical climate control on paleosol stacking patterns in the upper Paleocene–lower Eocene Willwood Formation, Bighorn Basin, Wyoming. Geology, **36**: 531–534; https://doi.org/10.1130/G24734A.1

Boulila, S., Galbrun, B., Hinnov, L.A., Collin, P.Y., Ogg, J.G., Fortwengler, D., Marchand, D., 2010. Milankovitch and sub-Milankovitch forcing of the Oxfordian (Late Jurassic) Terres Noires Formation (SE France) and global implications. Basin Research, **22**: 717–732; https://doi.org/10.1111/j.1365-2117.2009.00429.x

Bown, P.R., Rutledge, D.C., Crux, J.A., Gallagher, L.T., 1998. Lower Cretaceous. In: Calcareous Nannofossil Biostratigraphy (ed. P.R. Bown): 86–131. Kluwer Academic Publishers, Dordrecht.

Burtan, J., 1954. Szczegółowa Mapa Geologiczna Polski, 1:50 000, arkusz M34–Wieliczka (in Polish). Inst. Geol., Warszawa.

Burtan, J., 1966a. Szczegółowa Mapa Geologiczna Polski, 1:50 000, arkusz M34–77A Wieliczka Wieliczka (in Polish). Inst. Geol., Warszawa.

Burtan, J., 1966b. Szczegółowa Mapa Geologiczna Polski, 1:50 000, arkusz M34–77C Mszana Dolna Wieliczka (in Polish). Inst. Geol., Warszawa.

Burtan, J., 1978. Objaśnienia do Szczegółowej Mapy Geologicznej Polski, arkusz Mszana Dolna (1016), 1:50 000 Wieliczka (in Polish). Wydaw. Geol., Warszawa.

Cantalejo, B., Pickering, K.T., 2015. Orbital forcing as principal driver for fine-grained deep-marine siliciclastic sedimentation, Middle Eocene Ainsa Basin, Spanish Pyrenees. Palaeogeography, Palaeoclimatology, Palaeoecology, **421**: 24–47; https://doi.org/10.1016/j.palaeo.2015.01.008

Cantalejo, B., Pickering, K.T., Miller, K.G., Mac Niocaill, C., 2021. Chasing the 400 kyr pacing of deep-marine sandy submarine fans: Middle Eocene Aínsa Basin, Spanish Pyrenees. Journal of the Geological Society, **178,** jgs2019-173; https://doi.org/10.1144/jgs2019-173

Charbonnier, G., Boulila, S., Gardin, S., Duchamp-Alphonse, S., Adatte, T., Spangenberg, J.E., Föllmi, K.B., Colin, C., Galbrun, B., 2013. Astronomical calibration of the Valanginian "Weissert" episode: the Orpierre marl–limestone succession (Vocontian Basin, southeastern France). Cretaceous Research, **45:** 25–42; https://doi.org/10.1016/j.cretres.2013.07.003

Charbonnier, G., Duchamp-Alphonse, S., Adatte, T., Föllmi, K.B., Spangenberg, J.E., Gardin, S., Galbrun, B., Colin, C., 2016. Eccentricity-paced monsoon-like system along the northwestern Tethyan margin during the Valanginian (Early Cretaceous). Palaeogeography, Palaeoclimatology, Palaeoecology, **443:** 145–155; https://doi.org/10.1016/j.palaeo.2015.11.027

Chen, C., Hiscott, R.N., 1999. Statistical analysis of facies clustering in submarine-fan turbidite successions. Journal of Sedimentary Research, **69:** 505–517; https://doi.org/10.2110/jsr.69.505

Davis, J.C., 2002. Statistics and Data Analysis in Geology, 3rd ed. John Wiley & Sons, New York.

De Boor, C., 2001. A Practical Guide to Splines. Springer, New York.

Di Celma, C., 2011. Sedimentology, architecture, and depositional evolution of a coarse-grained submarine canyon fill from the Gelasian (early Pleistocene) of the Peri-Adriatic Basin, central Italy. Sedimentary Geology, **238:** 233–253; https://doi.org/10.1016/j.sedgeo.2011.05.003

Di Celma, C., Cantalamessa, G., 2012. Off-shelf sedimentary record of recurring global sea-level changes during the Plio-Pleistocene. Journal of the Geological Society, **169:** 643–646; https://doi.org/10.1144/jgs2012-041

Dżułyński, S., Walton, E.K., 1963. Experimental production of sole markings. Transactions of the Edinburgh Geological Society, **19:** 279–305; https://doi.org/10.1144/transed.19.3.279

Dżułyński, S., Książkiewicz, M., Kuenen, P.H., 1959. Turbidites in flysch of the Polish Carpathian Mountains. GSA Bulletin, **70:** 1089–1118; https://doi.org/10.1130/0016-7606(1959)70[1089:TIFOTP]2.0.CO;2

Egger, H., Schwerd, K., 2008. Stratigraphy and sedimentation rates of Upper Cretaceous deep-water systems of the Rhenodanubian Group (Eastern Alps, Germany). Cretaceous Research, **29:** 405–416; https://doi.org/10.1016/j.cretres.2007.03.002

Foucault, A., Powichrowski, L., Prud'homme, A., 1987. Le contrôle astronomique de la sédimentation turbiditique: exemple du Flysch à Helminthoïdes des Alpes Ligures (Italie). Comptes Rendus de l'Académie des Sciences, Paris, II, **305:** 1007–1011.

Geroch, S., 1966. Lower Cretaceous small foraminifera of the Silesian Series, Polish Carpathians (in Polish with English summary). Annales Societatis Geologorum Poloniae, **36:** 413–479.

Geroch, S., Nowak, W., 1984. Proposal of zonation for the Late Tithonian–Eocene based on arenaceous foraminifera from the Outer Carpathians, Poland. Bulletin des Centres de Recherches Exploration-Production Elf-Aquitaine, **6:** 225–239.

Ghil, M., Allen, M.R., Dettinger, M.D., Ide, K., Kondrashov, D., Mann, M.E., Robertson, A.W., Saunders, A., Tian, Y., Varadi, F., Yiou, P., 2002. Advanced spectral methods for climatic time series. Reviews of Geophysics, **40:** 1–40; https://doi.org/10.1029/2000RG000092

Giraud, F., Beaufort, L., Cotillon, P., 1995. Periodicities of carbonate cycles in the Valanginian of the Vocontian Trough: a strong obliquity control. Geological Society Special Publications, **85:** 143–164; https://doi.org/10.1144/GSL.SP.1995.085.01.09

Golonka, J., Krobicki, M., Matyszkiewicz, J., Olszewska, B., Ślączka, A., Słomka, T., 2005. Geodynamics of ridges and development of carbonate platforms within the Carpathian realm in Poland. Slovak Geological Magazine, **11:** 5–16.

Golonka, J., Waśkowska, A., Cieszkowski, M., Ślączka, A., Słomka, T., 2014. Geodynamics and palaeogeography of the Silesian Ridge in the Outer Carpathians. Proceedings of the XX Congress of the Carpathian-Balkan Geological Association, **1:** 315–318.

Haak, A.B., Schlager, W., 1989. Compositional variations in calciturbidites due to sea-level fluctuations, late Quaternary, Bahamas. Geologische Rundschau, **78:** 477–486; https://link.springer.com/article/10.1007/BF01776186

Hammer, Ø., Harper, D.A.T., Ryan, P.D., 2001. PAST: Paleontological statistics software package for education and data analysis. Palaeontologia Electronica, **4,** 9. https://palaeo-electronica.org/2001_1/past/past.pdf

Hammer, Ø., Harper, D.A.T., 2024. Paleontological Data Analysis. Blackwell Publishing, Malden.

Harding, I.C., 1986. An Early Cretaceous dinocyst assemblage from the Wealden of southern England. Special Papers in Palaeontology, **35:** 95–109.

Heard, T.G., Pickering, K.T., Robinson, S.A., 2008. Milankovitch forcing of bioturbation intensity in deep-marine thin-bedded siliciclastic turbidites. Earth and Planetary Science Letters, **272:** 130–138; https://doi.org/10.1016/j.epsl.2008.04.025

Hilgen, F.J., Hinnov, L.A., Aziz, H.A., Abels, H.A., Batenburg, S., Bosmans, J.H.C., Boer, B., Hüsing, S.K., Kuiper, K.F., Lourens, L.J., Rivera, T., Tuenter, E., Van de Wal, R.S.W., Wotzlaw, J.F., Zeeden, C., 2014. Stratigraphic continuity and fragmentary sedimentation: the success of cyclostratigraphy as part of integrated stratigraphy. Geological Society Special Publications, **404:** 157–197; https://doi.org/10.1144/SP404.12

Hinnov, L.A., 2000. New perspectives on orbitally forced stratigraphy. Annual Review of Earth and Planetary Sciences, **28:** 419–473; https://doi.org/10.1146/annurev.earth.28.1.419

Huang, H., Gao, Y.M.C., Jones, M.M., Zeeden, C., Ibarra, D.E., Wu, H., Wang, C., 2021. Organic carbon burial is paced by a ~173 ka obliquity cycle in the middle to high latitudes. Science Advances, **7,** eabf9489; https://doi.org/10.1126/sciadv.abf9489

Kędzierski, M., Ochabska, A., 2012. Calcareous nannofossil biostratigraphy and sedimentary environment of Valanginian–Hauterivian rhythmites (Silesian Nappe, Polish Carpathians). Annales Societatis Geologorum Poloniae, **82:** 225–237.

Klein, J., Busnardo, R., Company, M., Delanoy, G., Kakabadze, M., Reboulet, S., Ropol, P., Vašíček, Z., Vermeulen, J., 2007. Lower Cretaceous ammonites III. Bochianitoidea, Protancyloceratoidea, Ancyloceratoidea, Ptychoceratoidea. In: Fossilium Catalogus I: Animalia (ed. W. Riegraf), **144**. Backhuys Publishers, Leiden.

Kodama, K.P., Hinnov, L., 2015. Rock Magnetic Cyclostratigraphy. Wiley-Blackwell, Chichester; https://doi.org/10.1002/9781118561294

Kokoszyńska, B., 1949. Stratigraphy of the Lower Cretaceous in the northern Flysch Carpathians (in Polish with English summary). Prace Państwowego Instytutu Geologicznego, **6**.

Krijgsman, W., Langereis, C.G., Zachariasse, W.J., Boccaletti, M., Moratti, G., Gelati, R., Iaccarino, S., Papani, G., Villa, G., 1999. Late Neogene evolution of the Taza–Guercif Basin (Rifian Corridor, Morocco) and implications for the Messinian salinity crisis. Marine Geology, **153:** 147–160; https://doi.org/10.1016/S0025-3227(98)00084-X

Książkiewicz, M., 1951. Objaśnienia do ogólnej mapy geologicznej Polski, 1:50 000, arkusz Wadowice Wieliczka (in Polish). Państwowy Instytut geologiczny, Warszawa.

Książkiewicz, M., 1954. The Jurassic and Cretaceous of Bachowice (in Polish with English summary). Rocznik Polskiego Towarzystwa Geologicznego, **24:** 121–303; https://geojournals.pgi.gov.pl/asgp/article/view/10583/9075

Książkiewicz, M., 1956. Geology of the Northern Carpathians. Geologische Rundschau, **49:** 369–411; https://link.springer.com/article/10.1007/BF01802022

Leszczyński, S., 1997. Origin of the Sub-Menilite Globigerina Marl (Eocene–Oligocene transition) in the Polish Outer Carpathians. Annales Societatis Geologorum Poloniae, **67:** 367–427; https://geojournals.pgi.gov.pl/asgp/article/download/12300/10774

Lewis, K.B., Kohn, B.P., 1973. Ashes, turbidites, and rates of sedimentation on the continental slope off Hawkes Bay. New Zealand Journal of Geology and Geophysics, **16:** 439–454; https://doi.org/10.1080/00288306.1973.10431370

Li, M., Hinnov, L., Kump, L., 2019. Acycle: Time-series analysis software for paleoclimate research and education. Computers & Geosciences, **127**: 12–22; https://doi.org/10.1016/j.cageo.2019.02.011

Li, Y., Huang, H., Gao, Y., Cao, Y., Cheng, H., Hei, C., Liang, S., 2024. The ~170 kyr astronomical cycle in the Early Permian Lucaogou Formation of the Junggar Basin. Frontiers in Earth Science, **12**, 1272857; https://doi.org/10.3389/feart.2024.1272857

Liu, Y., Hinnov, L.A., Abadi, M.S., Huang, C., Zhou, Y., Zeeden, C., 2024. 30 million years of orbitally influenced sedimentation across the Jurassic–Cretaceous boundary and Early Cretaceous period. Marine and Petroleum Geology, **170**, 107092; https://doi.org/10.1016/j.marpetgeo.2024.107092

Longhitano, S.G., Nemec, W., 2005. Statistical analysis of bed-thickness variation in a Tortonian succession of biocalcarenitic tidal dunes, southern Italy. Sedimentary Geology, **179:** 195–224; https://doi.org/10.1016/j.sedgeo.2005.05.006

Mawson, M., Tucker, M., 2009. High-frequency cyclicity (Milankovitch and millennial-scale) in slope-apron carbonates: Zechstein (Upper Permian), NE England. Sedimentology, **56:** 1905–1936; https://doi.org/10.1111/j.1365-3091.2009.01062.x

Marwan, N., 2011. How to avoid potential pitfalls in recurrence plot-based data analysis. International Journal of Bifurcation and Chaos, **21:** 1003–1017; https://doi.org/10.48550/arXiv.1007.2215

Marwan, N., Romano, M.C., Thiel, M., Kurths, J., 2007. Recurrence plots for the analysis of complex systems. Physics Reports, **438:** 237–329; https://doi.org/10.1016/j.physrep.2006.11.001

Marwan, N., Donges, J.F., Donner, R.V., Eroglu, D., 2021. Nonlinear time series analysis of palaeoclimate proxy records. Quaternary Science Reviews, **274,** 107245; https://doi.org/10.1016/j.quascirev.2021.107245

Meyers, S.R., 2015. The evaluation of eccentricity-related amplitude modulation and bundling in paleoclimate data: An inverse approach for astrochronologic testing and time scale optimization. Paleoceanography, **30**: 1625–1640; https://doi.org/10.1002/2015PA002850

Meyers, S.R., Sageman, B.B., Arthur, M.A., 2012. Obliquity forcing of organic matter accumulation during Oceanic Anoxic Event 2. Paleoceanography, **27,** PA3212; https://doi.org/10.1029/2012PA002286

Mitchell, R.N., Gernon, T.M., Cox, G.M., Nordsvan, A.R., Kirscher, U., Xuan, C., Liu, Y., Liu, X., He, X., 2021. Orbital forcing of ice sheets during Snowball Earth. Nature Communications, **12,** 4187; https://doi.org/10.1038/s41467-021-24439-4

Mutterlose, J., Rawson, P.F., Reboulet, S., Baudin, F., Bulot, L., Emmanuel, L., Gardin, S., Martinez, M., Renard, M., 2021. The Global Boundary Stratotype Section and Point (GSSP) for the base of the Hauterivian Stage (Lower Cretaceous). Episodes, **44:** 129–150; https://doi.org/10.18814/epiiugs/2020/020072

Ninard, K., Uchman, A., Pieńkowski, G., Hesselbo, S.P., 2024. From Jurassic deep-sea life to deterministic Solar System dynamics. Volumina Jurassica, **22:** 25–34; https://doi.org/10.7306/VJ.22.3

Olszewska, B., Szydło, A., Jugowiec-Nazarkiewicz, M., Neścieruk, P., 2008. Integrated biostratigraphy of carbonate deposits of the Cieszyn Beds in the Polish Western Carpathians (in Polish with English summary). Geologia, **34:** 33–59.

Oszczypko, N., 2004. The structural position and tectonosedimentary evolution of the Polish Outer Carpathians. Przegląd Geologiczny, **52:** 780–791.

Payros, A., Martínez-Braceras, N., 2014. Orbital forcing in turbidite accumulation during the Eocene greenhouse interval. Sedimentology, **61:** 1411–1432; https://doi.org/10.1111/sed.12113

Payros, A., Martínez-Braceras, N., Dinarès-Turell, J., Bernaola, G., Monechi, S., 2023. The Lutetian GSSP at Gorrondatxe revisited. Palaeogeography, Palaeoclimatology, Palaeoecology, **625,** 111669; https://doi.org/10.1016/j.palaeo.2023.111669

Pickering, K.T., Bayliss, N.J., 2009. Deconvolving tectono-climatic signals in deep-marine siliciclastics. Geology, **37:** 203–206; https://doi.org/10.1130/G25261A.1

Pickering, K.T., Stow, D.A.V., Watson, M., Hiscott, R.N., 1986. Deep-water facies, processes and models. Earth-Science Reviews, **23:** 75–174; https://doi.org/10.1016/0012-8252(86)90001-2

Pickering, K.T., Souter, C., Oba, T., Taira, A., Schaaf, M., Platzman, E., 1999. Glacio-eustatic control on deep-marine clastic forearc sedimentation. Journal of the Geological Society, **156:** 125–136; https://doi.org/10.1144/gsjgs.156.1.0125

Pieńkowski, G., Uchman, A., Ninard, K., Page, K.N., Hesselbo, S.P., 2024. Early Jurassic extrinsic solar system dynamics versus intrinsic Earth processes. Progress in Earth and Planetary Science, **11,** 18; https://doi.org/10.1186/s40645-024-00612-3

Postma, G., Hilgen, F.J., Zachariasse, W.J., 1993. Precession-punctuated growth of a late Miocene submarine-fan lobe on Gavdos (Greece). Terra Nova, **5:** 438–444; https://doi.org/10.1111/j.1365-3121.1993.tb00281.x

Press, W.H., Teukolsky, S.A., Vetterling, W.T., Flannery, B.P., 1993. Numerical Recipes in FORTRAN. The Art of Scientific Computing, 2nd edition. Cambridge University Press, Cambridge.

Reboulet, S., Szives, O., Aguirre-Urreta, B., Barragán, R., Company, M., Frau, C., Kakabadze, M.V., Klein, J., Moreno-Bedmar, J.A., Lukeneder, A., Pictet, A., Ploch, I., Raisossadat, S.N., Vašíček, Z., Baraboshkin, E.J., Mitta, V.V., 2018. Report on the 6th International Meeting of the IUGS

Lower Cretaceous Ammonite Working Group. Cretaceous Research, **91:** 100–110; https://doi.org/10.1016/j.cretres.2018.05.008

Reijmer, J.J.G., Sprenger, A., Ten Kate, W.G.H.Z., Schlager, W., Krystyn, L., 1994. Periodicities in the composition of Late Triassic calciturbidites. IAS Special Publication, **19:** 323–343; https://doi.org/10.1002/9781444304039.ch21

Sepkoski, J.J., 2002. A Compendium of Fossil Marine Animal Genera. Bulletins of American Paleontology, **363**.

Spiridonov, A., 2017. Recurrence and cross-recurrence plots reveal the onset of the Mulde event (Silurian). Journal of Geology, **125:** 381–398; https://doi.org/10.1086/691184

Stampfli, G.M., Hochard, C., 2009. Plate tectonics of the Alpine realm. Geological Society Special Publications, **327:** 89–111; https://doi.org/10.1144/SP327.6

Sutcliffe, C., Pickering, K.T., 2009. End-signature of deep-marine basin fill. Sedimentology, **56:** 1670–1689; https://doi.org/10.1111/j.1365-3091.2009.01051.x

Szydło, A., 1996. Charakterystyka mikropaleontologiczna utworów dolnej kredy z rejonu Bielska-Białej i Żywca (in Polish). Posiedzenia Naukowe Państwowego Instytutu Geologicznego, **52:** 4.

Szymakowska, F., 1981. Stratigraphy of the Lower Cretaceous deposits of the Outer Flysch Carpathians based on ammonites (in Polish with English summary). Biuletyn Instytutu Geologicznego, **331:** 57–68.

Ślączka, A., Kruglov, S., Golonka, J., Oszczypko, N., Popadyuk, I., 2006. Geology and hydrocarbon resources of the Outer Carpathians. AAPG Memoir, **84:** 221–258; https://doi.org/10.1306/985610M843070

Ten Kate, W.G.H.Z., Sprenger, A., 1993. Orbital cyclicities above and below the Cretaceous/Paleogene boundary. Sedimentary Geology, **87:** 69–101; https://doi.org/10.1016/0037-0738(93)90037-6

Uchman, A., 1998. Taxonomy and ethology of flysch trace fossils. Annales Societatis Geologorum Poloniae, **68:** 105–218; https://geojournals.pgi.gov.pl/asgp/article/download/12322/10796

Uchman, A., 2004. Deep-sea trace fossils controlled by palaeo-oxygenation. Fossil and Strata, **51:** 39–57; https://doi.org/10.18261/9781405169851-2004-03

Uchman, A., 2008. Poznachowice Dolne – Upper Cieszyn Beds and Grodziszcze Beds. In: Ichnological Sites of Poland (eds. G. Pieńkowski and A. Uchman): 140–141. Polish Geological Institute, Warsaw.

Uchman, A., Szczęch, M., 2022. Poznachowice Górne – Krzyworzeka river section. In: Cretaceous of Poland and Adjacent Areas (eds. I. Walaszczyk and J.P. Todes): 274–276. University of Warsaw, Warsaw.

Uchman, A., Kuźma, A., Szczęch, M., 2023. Poznachowice Górne – profil Krzyworzeki (in Polish). In: LXXXVIII Zjazd Naukowy Polskiego Towarzystwa Geologicznego: 86–90. Polish Geological Society, Kraków.

Vašíček, Z., Gedl, E., Kędzierski, M., Uchman, A., 2010. Two ammonites from the Early Cretaceous deep-sea sediments of the Silesian Nappe. Annales Societatis Geologorum Poloniae, **80:** 25–37.

Weedon, G.P., 2003. Time-Series Analysis and Cyclostratigraphy. Cambridge University Press, Cambridge; https://doi.org/10.1017/CBO9780511535482

Weedon, G.P., 2022. Problems with the current practice of spectral analysis in cyclostratigraphy: avoiding false detection of regular cyclicity. Earth-Science Reviews, **235**, 104261; https://doi.org/10.1016/j.earscirev.2022.104261

Weedon, G.P., Page, K.N., Jenkyns, H.C., 2019. Cyclostratigraphy, stratigraphic gaps and the duration of the Hettangian Stage (Jurassic): Insights from the Blue Lias Formation of southern Britain. Geological Magazine, **156:** 1469–1509; https://doi.org/10.1017/S0016756818000808

Weltje, G.J., de Boer, P.L., 1993. Astronomically induced palaeoclimatic oscillations in Pliocene turbidites. Geology, **21:** 307–310; https://doi.org/10.1130/0091-7613(1993)021%3C0307:AIPORI%3E2.3.CO;2

Weron, R., 2002. Estimating long-range dependence. Physica A, **312:** 285–299; https://doi.org/10.1016/S0378-4371(02)00961-5

Wu, H., Zhang, S., Feng, Q., Jiang, G., Li, H., Yang, T., 2012. Milankovitch and sub-Milankovitch cycles of the Early Triassic Daye Formation. Gondwana Research, **22:** 748–759; https://doi.org/10.1016/j.gr.2011.12.003

Yao, X., Hinnov, L.A., 2019. Advances in characterizing the cyclostratigraphy of binary chert-mudstone lithologic successions, Permian (Roadian–lower Capitanian), Chaohu, Lower Yangtze, South China. Palaeogeography, Palaeoclimatology, Palaeoecology, **528**: 258–271; https://doi.org/10.1016/j.palaeo.2019.05.004

Yao, X., Dai, S., Li, M., Hinnov, L., 2022. Orbital eccentricity and inclination metronomes in Middle Miocene lacustrine mudstones. Global and Planetary Change, **215,** 103896; https://doi.org/10.1016/j.gloplacha.2022.103896

Zeeden, C., Laskar, J., De Vleeschouwer, D., Pas, D., Da Silva, A.C., 2023. Earth's rotation and Earth–Moon distance in the Devonian. Earth and Planetary Science Letters, **621,** 118348; https://doi.org/10.1016/j.epsl.2023.118348

Zhang, Y., Fang, Q., Wu, H., Shi, M., Gai, C., Zhang, S., Yang, T., Li, H., Zeeden, C., 2025. Cambrian millennial-scale climate cycles paced by Milanković forcing. Global and Planetary Change, **253,** 104988; https://doi.org/10.1016/j.gloplacha.2025.104988

Zhang, Z., Zhang, K., Khelifi, A., 2018. Multivariate Time Series Analysis in Climate and Environmental Research. Springer, Cham.

SOFTWARE:

Marwan, N. Cross Recurrence Plot Toolbox for MATLAB, Version 5.29 (R38)

APPENDIX 1A. Bed thickness dataset

Thickness [m]	Depth [m]	Facies assigned
0.078	0.078	F2
0.709	0.787	F1
0.038	0.825	F4
0.203	1.028	F1
0.016	1.044	F2
0.228	1.272	F1
0.031	1.303	F4
0.044	1.347	F1
0.105	1.452	F2
0.47	1.922	F1
0.01	1.932	F4
0.135	2.067	F1
0.055	2.122	F4
0.04	2.162	F1
0.415	2.577	-
0.135	2.712	F2
0.082	2.794	F1
0.051	2.845	F4
0.04	2.885	F2
0.027	2.912	F1
0.015	2.927	F4
0.08	3.007	F1
0.043	3.05	F4
0.06	3.11	F1
0.205	3.315	F2
0.09	3.405	F1
0.01	3.415	F4
0.417	3.832	F4
0.17	4.002	-
0.03	4.032	F4
0.04	4.072	F1
0.04	4.112	F4
0.145	4.257	F1
0.067	4.324	F4
0.123	4.447	F1
0.02	4.467	F4
0.133	4.6	F1
0.065	4.665	F4
0.085	4.75	F1
0.045	4.795	F4
0.048	4.843	F1
0.025	4.868	F4
0.15	5.018	F1
0.03	5.048	F4
0.035	5.083	F1
0.04	5.123	F4
0.1	5.223	F1
0.02	5.243	F4
0.23	5.473	F1
0.02	5.493	F4
0.08	5.573	F1
0.03	5.603	F4
0.195	5.798	F1
0.185	5.983	F4
0.075	6.058	F2
0.12	6.178	F4
0.135	6.313	F1
0.05	6.363	F4
0.055	6.418	F1
0.11	6.528	F4
0.44	6.968	F1
0.055	7.023	F4
0.045	7.068	F1
0.053	7.121	F4
0.045	7.166	F1
0.115	7.281	F4
0.183	7.464	F1
0.16	7.624	F2
0.035	7.659	F4
0.055	7.714	F1
0.02	7.734	F4
0.022	7.756	F1
0.015	7.771	F4
0.075	7.846	F1
0.02	7.866	F4
0.05	7.916	F1
0.03	7.946	F4
0.2	8.146	F1
0.015	8.161	F4
0.04	8.201	F1
0.043	8.244	F4
0.055	8.299	F1
0.05	8.349	F4

0.124	8.473	F1
0.095	8.568	F4
0.18	8.748	F1
0.08	8.828	F2
0.035	8.863	F4
0.032	8.895	F1
0.025	8.92	F4
0.08	9	F1
0.025	9.025	F4
0.203	9.228	F1
0.03	9.258	F4
0.095	9.353	F1
0.015	9.368	F4
0.045	9.413	F1
0.035	9.448	F4
0.17	9.618	F1
0.045	9.663	F4
0.175	9.838	F1
0.045	9.883	F4
0.04	9.923	F1
0.126	10.049	F4
0.215	10.264	F1
0.053	10.317	F4
0.087	10.404	F1
0.028	10.432	F4
0.32	10.752	F1
0.06	10.812	F4
0.26	11.072	F1
0.06	11.132	F4
0.14	11.272	F1
0.055	11.327	F4
0.03	11.357	F1
0.08	11.437	F4
0.04	11.477	F1
0.1	11.577	F4
0.093	11.67	F1
0.042	11.712	F4
0.172	11.884	F1
0.04	11.924	F4
0.168	12.092	F1
0.026	12.118	F4
0.228	12.346	F1
0.1	12.446	F2
1.4	13.846	F1
0.03	13.876	F4
0.185	14.061	F1
0.05	14.111	F4
0.088	14.199	F1
0.03	14.229	F4
0.152	14.381	F1
0.135	14.516	F4
0.105	14.621	F1
0.1	14.721	F4
0.16	14.881	F1
0.102	14.983	F4
0.02	15.003	F2
0.585	15.588	F1
0.17	15.758	F4
0.335	16.093	F1
0.065	16.158	F4
0.27	16.428	F1
0.215	16.643	F4
0.27	16.913	F1
0.215	17.128	F4
0.295	17.423	F1
0.075	17.498	F4
0.085	17.583	F1
0.03	17.613	F4
0.17	17.783	F1
0.02	17.803	F4
0.045	17.848	F1
0.015	17.863	F4
0.3	18.163	F1
0.09	18.253	F4
0.17	18.423	F1
0.02	18.443	F4
0.28	18.723	F1
0.06	18.783	F4
0.55	19.333	F1
0.125	19.458	F4
0.425	19.883	F1
0.03	19.913	F4
0.3	20.213	F1
0.043	20.256	F4
0.305	20.561	F1
0.02	20.581	F4
0.14	20.721	F1
0.11	20.831	F4

0.26	21.091	F1
0.085	21.176	F4
0.205	21.381	F1
0.185	21.566	F4
0.395	21.961	F1
0.03	21.991	F4
0.14	22.131	F1
0.05	22.181	F4
0.39	22.571	F1
0.1	22.671	F4
0.06	22.731	F4
0.341	23.072	F1
0.15	23.222	F4
0.314	23.536	F1
0.046	23.582	F4
0.47	24.052	F1
0.12	24.172	F4
0.375	24.547	F1
0.028	24.575	F4
0.32	24.895	F1
0.04	24.935	F4
0.635	25.57	F1
0.025	25.595	F4
0.27	25.865	F1
0.065	25.93	F4
0.51	26.44	F1
0.075	26.515	F4
1.17	27.685	F1
0.03	27.715	F4
0.56	28.275	F1
0.055	28.33	F4
0.178	28.508	F1
0.03	28.538	F4
0.34	28.878	F1
0.09	28.968	F4
0.4	29.368	F1
0.565	29.933	F2
0.165	30.098	F2
0.15	30.248	F1
0.155	30.403	F4
0.34	30.743	F1
0.038	30.781	F4
0.79	31.571	F1
0.055	31.626	F4

0.103	31.729	F1
0.039	31.768	F2
0.77	32.538	F1
0.06	32.598	F4
0.695	33.293	F1
0.02	33.313	F2
0.48	33.793	F1
0.053	33.846	F4
0.86	34.706	F1
0.03	34.736	F4
0.023	34.759	F1
0.115	34.874	F2
0.145	35.019	F1
0.16	35.179	F4
0.735	35.914	F1
0.035	35.949	F4
1.18	37.129	F1
0.034	37.163	F4
0.355	37.518	F1
0.05	37.568	F4
0.05	37.618	F2
1.59	39.208	F1
0.045	39.253	F4
0.615	39.868	F1
0.29	40.158	F3
0.28	40.438	F1
0.043	40.481	F4
0.11	40.591	F1
0.02	40.611	F4
1.04	41.651	F1
0.185	41.836	F2
0.555	42.391	F1
0.04	42.431	F4
0.455	42.886	F1
0.018	42.904	F4
0.105	43.009	F1
0.075	43.084	F4
0.035	43.119	F1
0.085	43.204	F2
2.23	45.434	F1
0.043	45.477	F2
1.13	46.607	F1
0.19	46.797	F3
0.62	47.417	F1

0.06	47.477	F4
0.05	47.527	F1
0.085	47.612	F2
2.095	49.707	F1
0.045	49.752	F2
0.07	49.822	F4
0.465	50.287	F1
0.04	50.327	F2
0.96	51.287	F1
0.038	51.325	F4
0.86	52.185	F1
0.04	52.225	F3
0.07	52.295	F1
0.06	52.355	F3
0.355	52.71	F1
0.09	52.8	F2
0.58	53.38	F1
0.02	53.4	F4
0.53	53.93	F1
0.1	54.03	F2
1.07	55.1	F1
0.14	55.24	F2
0.35	55.59	F4
0.35	55.94	F1
0.04	55.98	F4
0.51	56.49	F1
0.1	56.59	F3
0.435	57.025	F1
0.02	57.045	F4
1.2	58.245	F1
0.02	58.265	F2
0.43	58.695	F1
0.02	58.715	F2
0.16	58.875	F4
0.5	59.375	F1
0.16	59.535	F3
0.45	59.985	F1
0.03	60.015	F4
0.63	60.645	F1
0.11	60.755	F4
0.67	61.425	F1
1.12	62.545	F1
0.25	62.795	F4
0.83	63.625	F1
0.16	63.785	F4
0.11	63.895	F1
0.07	63.965	F4
0.82	64.785	F1
0.01	64.795	F4
0.42	65.215	F1
0.03	65.245	F4
0.28	65.525	F1
0.02	65.545	F4
1.16	66.705	F1
0.25	66.955	F1
0.1	67.055	F4
0.51	67.565	F1
0.02	67.585	F4
0.61	68.195	F1
0.09	68.285	F4
0.5	68.785	F1
0.05	68.835	F4
0.048	68.883	F1
0.02	68.903	F4
0.095	68.998	F1
0.02	69.018	F2
0.99	70.008	F1
0.02	70.028	F4
1.03	71.058	F1
0.2	71.258	F2
0.99	72.248	F1
0.04	72.288	F4
0.41	72.698	F1
0.02	72.718	F4
0.87	73.588	F1
0.02	73.608	F4
0.78	74.388	F1
0.03	74.418	F4
0.08	74.498	F1
0.03	74.528	F4
0.11	74.638	F2
1	75.638	F1
0.03	75.668	F4
0.0527	75.721	F1
0.05	75.771	F4
0.9	76.671	F1
0.04	76.711	F2
0.21	76.921	F1

0.085	77.006	F4
0.45	77.456	F1
0.11	77.566	F2
0.18	77.746	F1
0.04	77.786	F2
1.02	78.806	F1
0.04	78.846	F4
0.49	79.336	F1
0.04	79.376	F4
1.4	80.776	F1
0.32	81.096	F2
0.21	81.306	F4
0.79	82.096	F1
0.1	82.196	F4
0.68	82.876	F1
0.035	82.911	F4
0.57	83.481	F1
0.13	83.611	F4
0.55	84.161	F1
0.08	84.241	F4
0.23	84.471	F1
0.53	85.001	F4
0.18	85.181	F1
0.1	85.281	F5
0.4	85.681	F1
0.02	85.701	F2
0.425	86.126	F1
0.32	86.446	F3
0.43	86.876	F1
0.09	86.966	F5
0.345	87.311	F1
0.055	87.366	F5
0.255	87.621	F1
0.245	87.866	F3
0.465	88.331	F1
0.19	88.521	F3
0.3	88.821	F1
0.06	88.881	F5
3.64	92.521	-
0.46	92.981	F1
0.04	93.021	F4
0.26	93.281	F1
0.12	93.401	F4
0.1	93.501	F5
0.19	93.691	F1
0.07	93.761	F4
0.5	94.261	F1
0.05	94.311	F4
0.94	95.251	F1
0.06	95.311	F5
0.115	95.426	F1
0.06	95.486	F4
0.8	96.286	F1
0.045	96.331	F5
0.33	96.661	F1
0.53	97.191	F4
0.77	97.961	F1
0.03	97.991	F3
1.32	99.311	F1
0.42	99.731	F2
1.58	101.311	F1
0.13	101.441	F4
1.04	102.481	F1
0.09	102.571	F5
0.42	102.991	F1
0.1	103.091	F5
0.58	103.671	F1
0.04	103.711	F4
0.14	103.851	F1
0.025	103.876	F4
2.15	106.026	-
0.06	106.086	F2
0.08	106.166	F4
2.66	108.826	F1
0.15	108.976	F4
1.03	110.006	F1
0.06	110.066	F2
0.78	110.846	F1
0.18	111.026	F2
1.41	112.436	F1
0.055	112.491	F4
0.91	113.401	F1
0.015	113.416	F4
0.25	113.666	F1
0.03	113.696	F4
0.16	113.856	F2
1.02	114.876	F1
0.04	114.916	F4

0.36	115.276	F1
0.4	115.676	F4
0.26	115.936	F1
0.03	115.966	F2
0.45	116.416	F1
0.04	116.456	F5
0.06	116.516	F1
0.035	116.551	F5
0.78	117.331	F1
0.115	117.446	F5
0.14	117.586	F1
0.05	117.636	F5
0.74	118.376	F1
0.04	118.416	F4
0.15	118.566	F1
0.05	118.616	F4
0.47	119.086	F1
0.07	119.156	F5
0.2	119.356	F1
0.03	119.386	F4
0.2	119.586	F1
0.02	119.606	F4
0.06	119.666	F1
0.025	119.691	F4
0.105	119.796	F1
0.02	119.816	F4
0.36	120.176	F1
0.11	120.286	F4
0.26	120.546	F1
0.51	121.056	F4
0.47	121.526	F1
0.095	121.621	F2
0.66	122.281	F1
0.045	122.326	F2
0.185	122.511	F1
0.19	122.701	F4
0.25	122.951	F1
0.14	123.091	F4
0.15	123.241	F1
0.03	123.271	F4
0.38	123.651	F1
0.12	123.771	F5
0.41	124.181	F1
0.045	124.226	F4
0.33	124.556	F1
0.03	124.586	F4
0.6	125.186	F1
0.05	125.236	F5
0.285	125.521	F1
0.11	125.631	F5
0.6	126.231	F1
0.46	126.691	F3
2.14	128.831	F1
0.18	129.011	F4
0.315	129.326	F1
0.03	129.356	F4
0.28	129.636	F1
0.08	129.716	F4
0.11	129.826	F1
0.26	130.086	F4
0.27	130.356	F1
0.04	130.396	F4
0.21	130.606	F1
0.23	130.836	F4
0.14	130.976	F4
0.16	131.136	F2
0.2	131.336	F1
0.025	131.361	F4
0.11	131.471	F1
0.02	131.491	F4
0.175	131.666	F1
0.02	131.686	F4
0.4	132.086	F1
0.02	132.106	F4
0.19	132.296	F1
0.09	132.386	F4
0.61	132.996	F1
0.18	133.176	F4
0.45	133.626	F1
0.59	134.216	F3
0.53	134.746	F4
0.09	134.836	F5
0.08	134.916	F1
0.12	135.036	F4
0.16	135.196	F1
0.08	135.276	F4
0.12	135.396	F1
0.06	135.456	F2

0.55	136.006	F1
0.08	136.086	F5
0.17	136.256	F1
0.11	136.366	F2
0.2	136.566	F1
0.05	136.616	F5
1.19	137.806	F1
1.9	139.706	F1
0.24	139.946	F4
0.32	140.266	F3
0.48	140.746	F1
0.12	140.866	F5
0.21	141.076	F3
0.05	141.126	F1
0.14	141.266	F5
0.19	141.456	F1
0.16	141.616	F4
1.23	142.846	F1
0.03	142.876	F4
0.43	143.306	F1
0.05	143.356	F4
0.105	143.461	F1
0.04	143.501	F4
0.32	143.821	F1
0.03	143.851	F4
0.12	143.971	F1
0.03	144.001	F4
0.25	144.251	F1
1.1	145.351	F3
0.31	145.661	F1
0.03	145.691	F4
0.89	146.581	F1
0.2	146.781	F5
0.64	147.421	F1
0.15	147.571	F5
0.1	147.671	F1
0.08	147.751	F4
0.52	148.271	F1
0.14	148.411	F5
0.31	148.721	F1
0.15	148.871	F5
0.64	149.511	F1
0.03	149.541	F4
0.58	150.121	F1
0.07	150.191	F5
0.17	150.361	F1
0.07	150.431	F2
0.28	150.711	F1
0.03	150.741	F4
0.37	151.111	F1
0.1	151.211	F3
0.7	151.911	F1
0.39	152.301	F4
0.39	152.691	F1
0.52	153.211	F3
0.5	153.711	F1
0.09	153.801	F5
0.17	153.971	F4
0.19	154.161	F1
0.04	154.201	F5
1.09	155.291	F1
0.1	155.391	F4
0.1	155.491	F1
0.06	155.551	F4
0.42	155.971	F1
0.03	156.001	F4
0.155	156.156	F1
0.07	156.226	F4
0.68	156.906	F1
0.15	157.056	F4
0.77	157.826	F1
0.12	157.946	F3
0.28	158.226	F1
0.08	158.306	F4
0.18	158.486	F1
0.3	158.786	F4
0.25	159.036	F1
0.25	159.286	F4
0.63	159.916	F1
0.11	160.026	F5
0.22	160.246	F1
0.04	160.286	F4
1.29	161.576	F1
0.17	161.746	F1
0.03	161.776	F4
0.06	161.836	F2
1.4	163.236	F1
0.02	163.256	F5

0.14	163.396	F1
0.06	163.456	F2
0.02	163.476	F4
0.2	163.676	F1
1.46	165.136	F1
0.04	165.176	F4
0.51	165.686	F1
0.01	165.696	F1
0.8	166.496	F1
0.09	166.586	F4
0.87	167.456	F1
0.51	167.966	F4
1.68	169.646	F1
0.02	169.666	F4
0.97	170.636	F1
0.04	170.676	F4
0.31	170.986	F1
0.04	171.026	F4
0.23	171.256	F1
0.03	171.286	F4
0.67	171.956	F1
1.69	173.646	F4
0.14	173.786	F5
0.67	174.456	F1
0.02	174.476	F4
1.07	175.546	F1
0.53	176.076	F1
0.16	176.236	F5
1.32	177.556	F1
2	179.556	-
0.72	180.276	F1
1.54	181.816	F4
3	184.816	-
0.84	185.656	F4
1.03	186.686	F1
1.03	187.716	F4
0.2	187.916	F5
0.27	188.186	F1
0.02	188.206	F4
0.07	188.276	F1
0.04	188.316	F4
0.08	188.396	F1
0.06	188.456	F4
0.58	189.036	F1

0.01	189.046	F4
0.2	189.246	F1
0.07	189.316	F4
0.1	189.416	F1
0.04	189.456	F4
0.08	189.536	F1
0.02	189.556	F4
0.14	189.696	F1
0.1	189.796	F5
0.09	189.886	F1
0.02	189.906	F4
0.31	190.216	F1
0.2	190.416	F4
0.25	190.666	F1
0.17	190.836	F4
0.09	190.926	F1
0.06	190.986	F4
0.18	191.166	F1
0.02	191.186	F4
0.25	191.436	F1
0.19	191.626	F4
0.42	192.046	F1
0.05	192.096	F4
0.06	192.156	F2
0.24	192.396	F1
0.035	192.431	F4
0.2	192.631	F1
0.02	192.651	F4
0.3	192.951	F1
0.15	193.101	F4
0.09	193.191	F1
0.11	193.301	F4
0.085	193.386	F1
0.055	193.441	F4
0.61	194.051	F1
0.025	194.076	F4
0.19	194.266	F1
0.06	194.326	F4
0.56	194.886	F1
0.035	194.921	F4
0.27	195.191	F1
0.03	195.221	F4
0.68	195.901	F1
0.14	196.041	F4

0.02	196.061	F2
0.19	196.251	F1
0.02	196.271	F4
0.68	196.951	F1
0.74	197.691	F2
1.67	199.361	F1
0.02	199.381	F4
1.01	200.391	F1
0.015	200.406	F4
0.73	201.136	F1
0.02	201.156	F4
0.61	201.766	F1
1.2	202.966	-
0.39	203.356	F1
0.2	203.556	F2
1.41	204.966	F1

0.32	205.286	F3
0.2	205.486	F1
0.33	205.816	F2
1.89	207.706	F1
0.03	207.736	F3
0.31	208.046	F1
0.19	208.236	F2
2.7	210.936	F1
1.08	212.016	F2
0.57	212.586	F1
4.1	216.686	F2
1.37	218.056	F1
0.04	218.096	F3
0.87	218.966	F1
1.03	219.996	F2

APPENDIX 1B1. Facies description summary

FACIES	DESCRIPTION
Facies F1	Calcareous mudstones interbedded with very-thin bedded, fine-grained, and very fine-grained calcareous sandstones (mudstones prevailing); mudstones 5 to 150 mm thick (hemipelagic ones up to 3 mm), sandstones 1 to 30 mm thick
Facies F2	Rusty colour beds of mudstones, siltstones, and sandstones, thin and medium-bedded (1 to 30 cm thick).
Facies F3	Massive sandstones and conglomerates with exotic clasts often appearing as concave-plane lensoidal beds with a maximum thickness of 110 cm.
Facies F4	Fine- and medium-grained sandstones interbedded with mudstones, similar to F1, but sandstones predominate. Mudstone beds are 5–30 mm thick, and sandstones are 10–50 mm thick.
Facies F5	Laterally continuous beds of medium- and coarse-grained sandstones with cross and parallel lamination, and massive conglomerates (beds are 5–20 cm thick)

APPENDIX 1B2. Results of runs test

	H_0 = F1 random	H_0 = F2 random	H_0 = F3 random	H_0 = F4 random	H_0 = F5 random
N_1	619	2065	2146	1933	2167
N_2	1581	134	53	266	32
Number of 'runs'	432	92	35	291	57
Expected number of 'runs'	889.64	252.67	104.45	468.65	64.069
Z value	-24.158	-29.99	-31.627	-17.829	-5.2967
H_0 probability	6.196×10^{-129}	1.3135×10^{-197}	1.5816×10^{-219}	4.2349×10^{-71}	1.1789×10^{-07}
H_0 rejected?	yes	yes	yes	yes	yes

APPENDIX 1B3. Model typologies of recurrence plots (right) based on particular signals (left). After Coco and Dale (2014); Ninard et al. (2024); modified

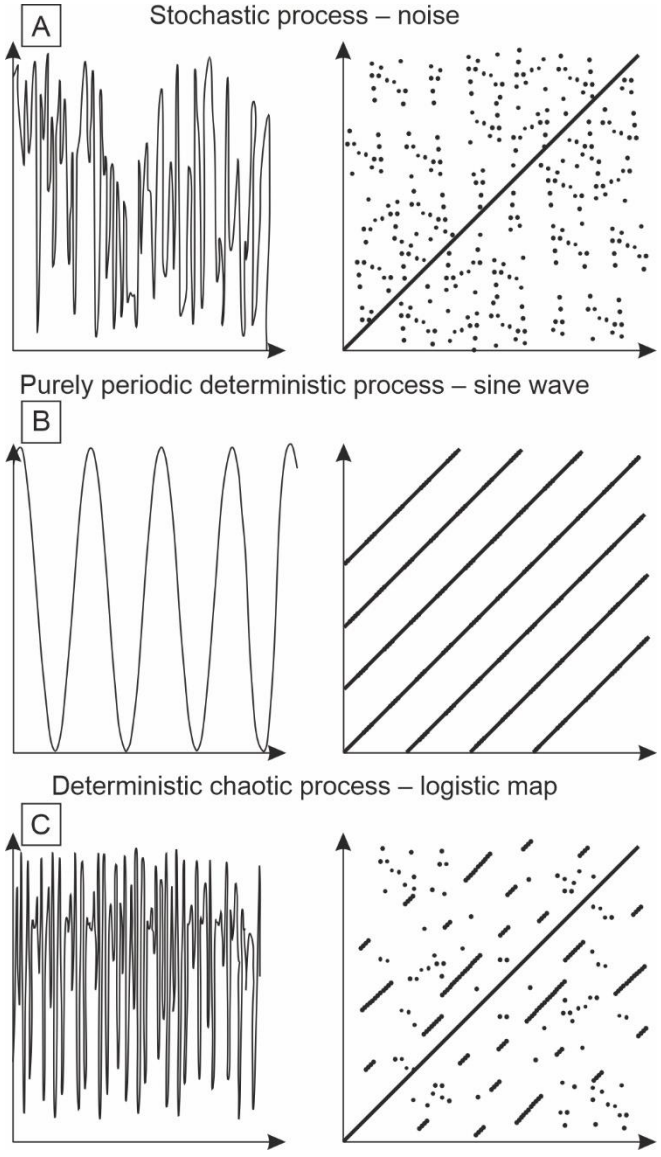

APPENDIX 1C. Recurrence plots representing the repeatability of facies F1 and F4

Cross Recurrence Plot facies F1
Dimension: 5, Delay: 10, Threshold: 20% (interdependent neighbours)

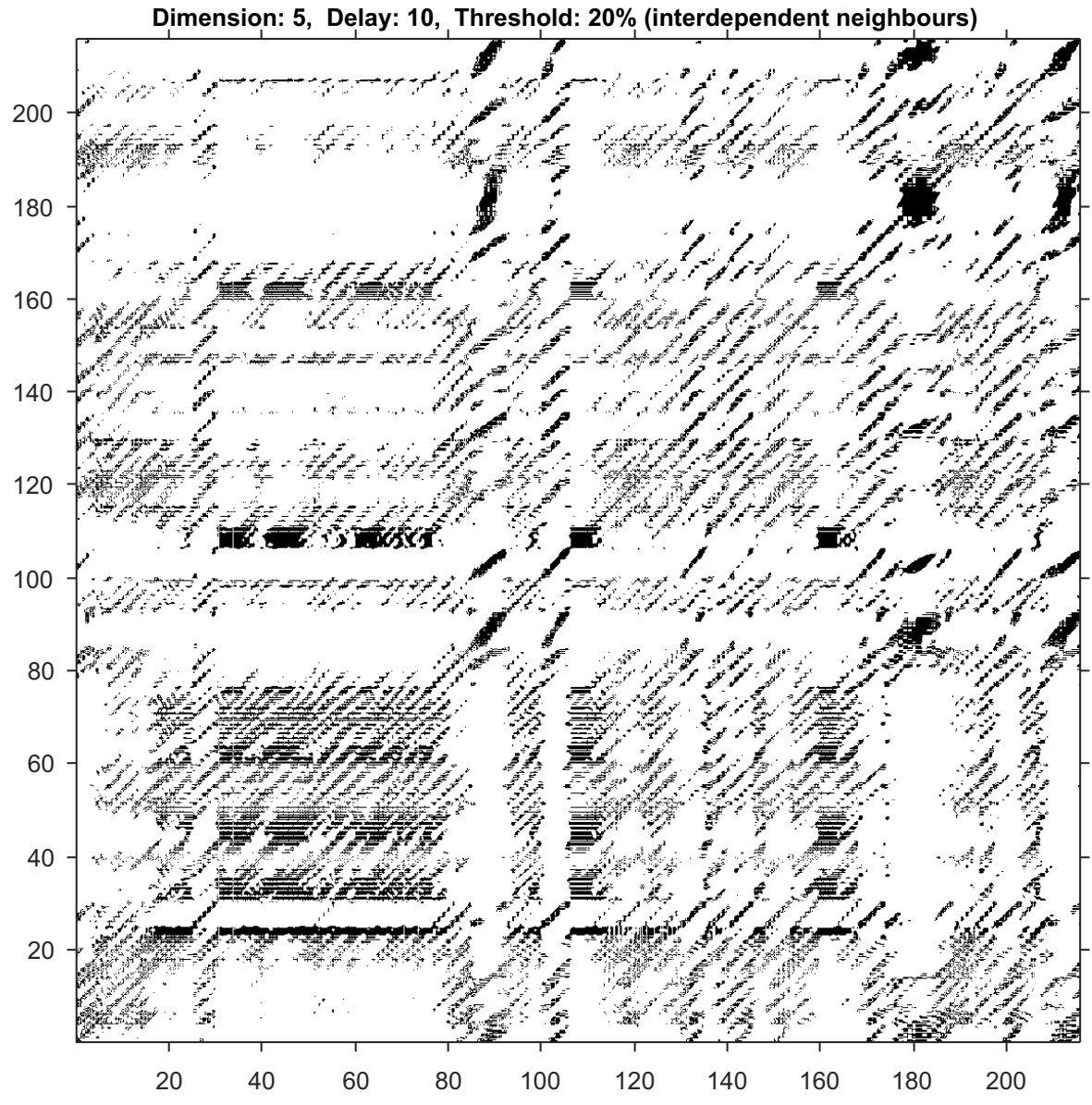

Cross Recurrence Plot facies F4
Dimension: 8, Delay: 10, Threshold: 10% (interdependent neighbours)

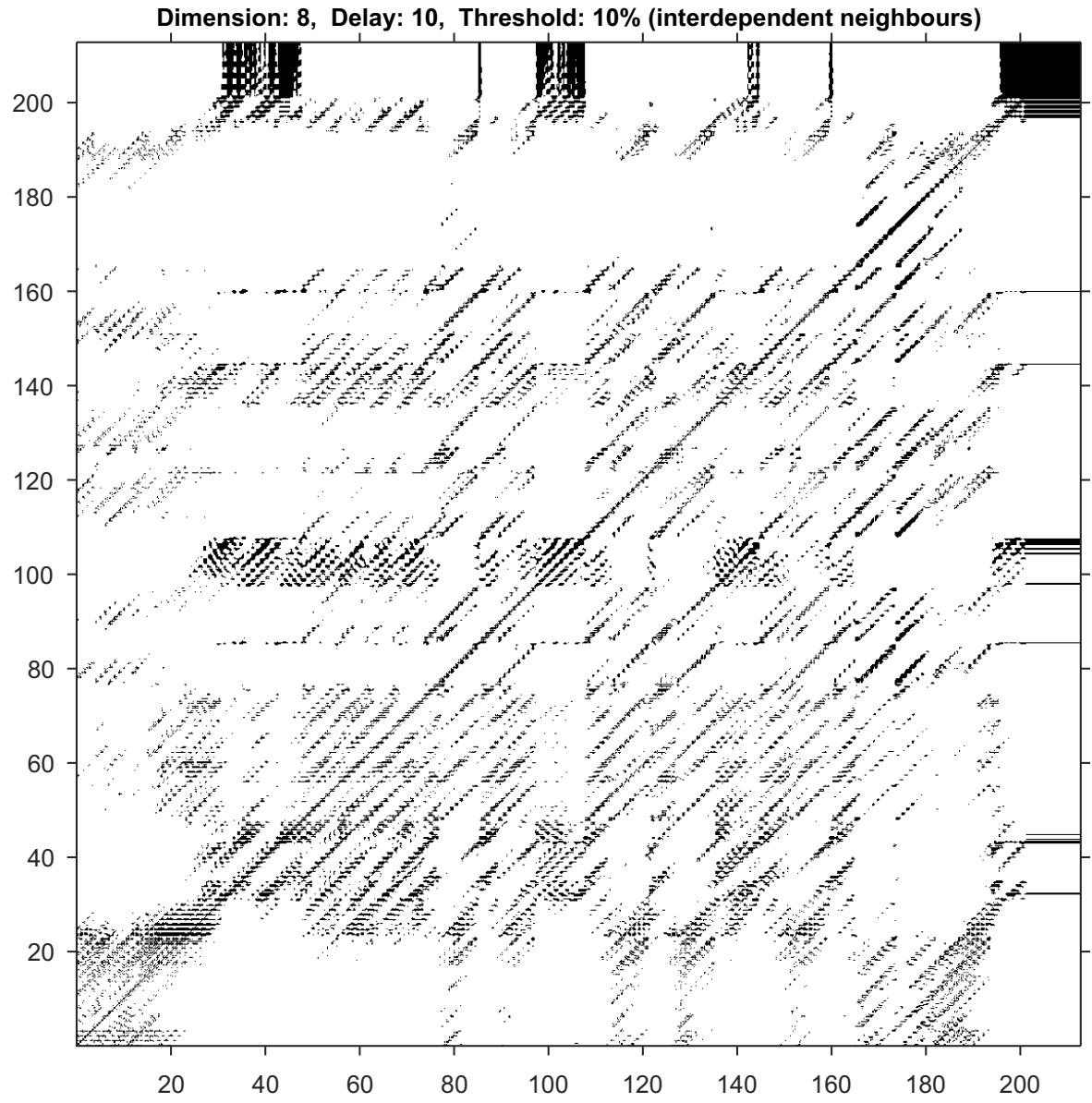

Cross Recurrence Plot facies F5
Dimension: 20, Delay: 11, Threshold: 10% (interdependent neighbours)

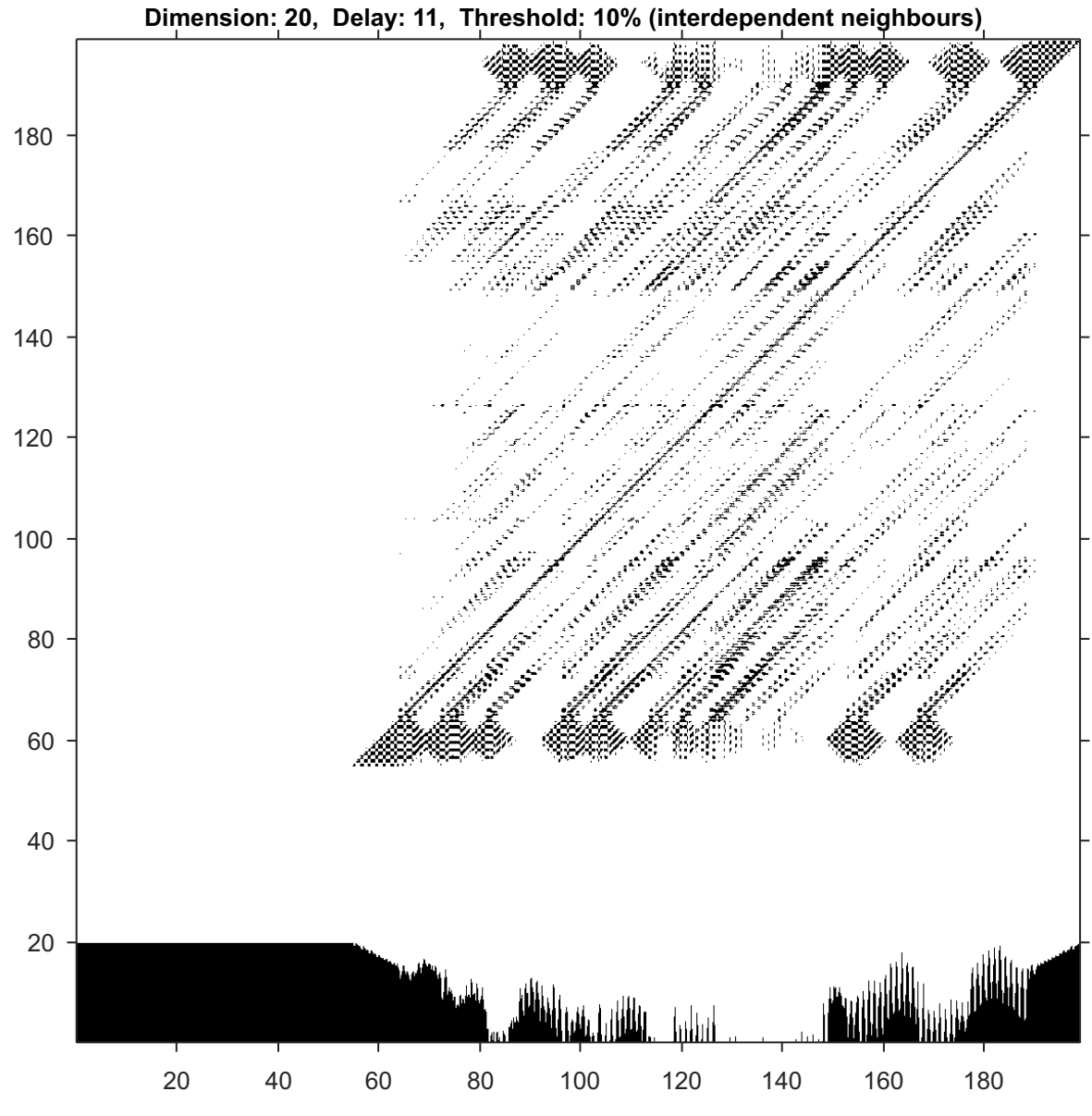

APPENDIX 1D1. Evolutive spectrum based on the smoothed Facies F2 occurrence time series – the same data as used for recurrence plot quantification. Dominant wavelengths occur at circa 5.2 m, 7.4 m and 18-25 m

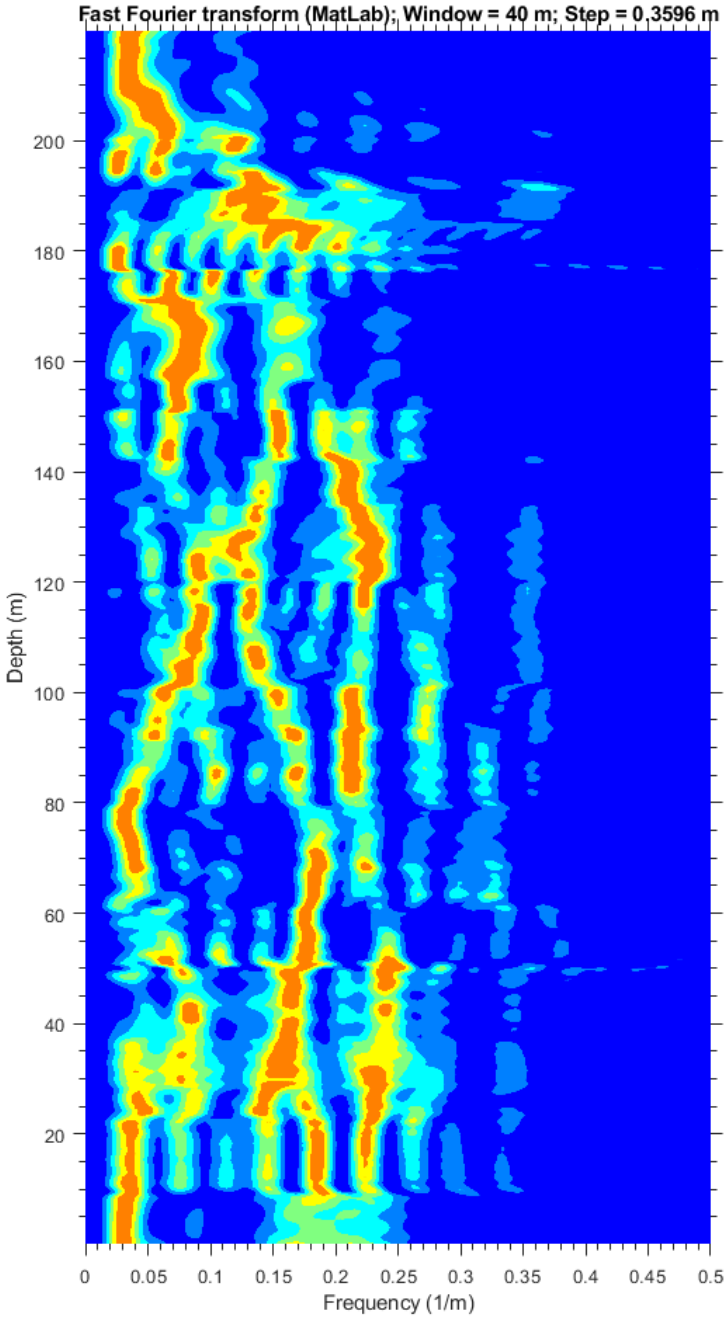

APPENDIX 1D2. Evolutive spectrum based on the smoothed Facies F3 occurrence time series – the same data as used for recurrence plot quantification. Dominant stable wavelengths occur at circa 7.4 m and 18-25 m

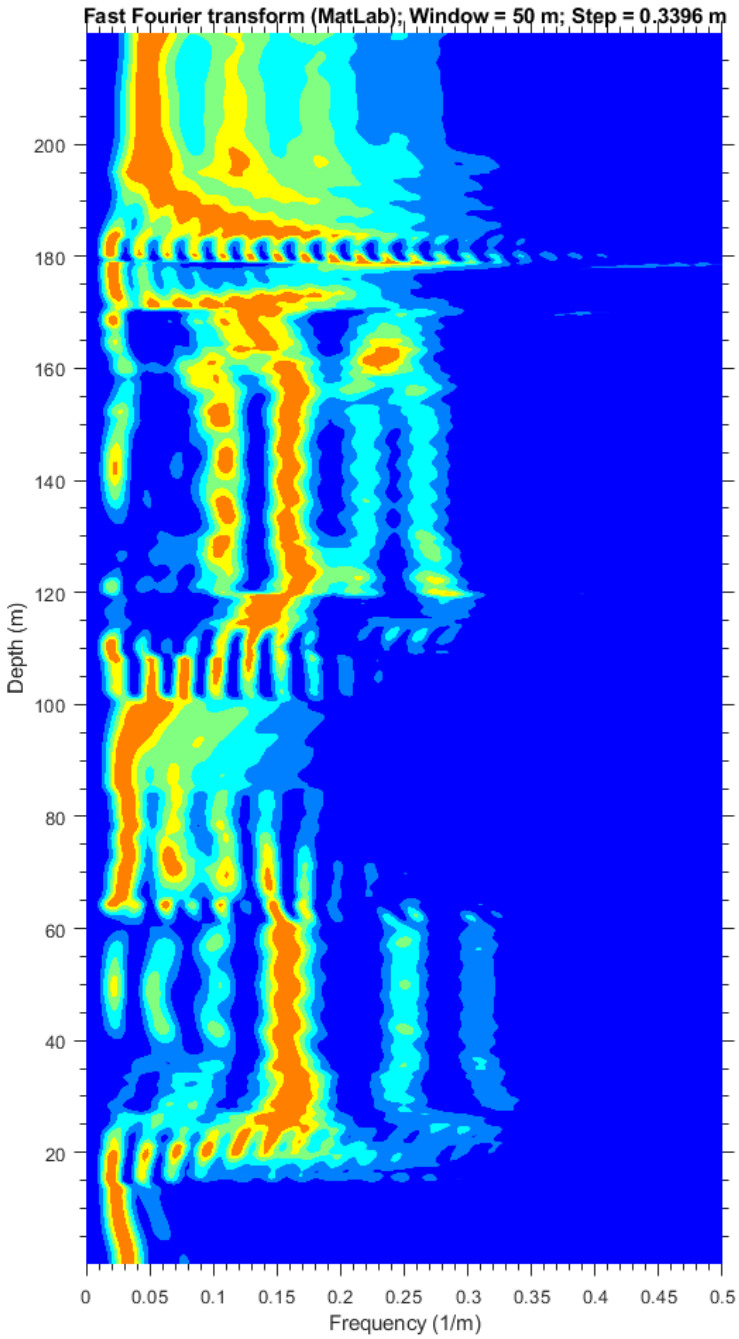

APPENDIX 1D3. Evolutive spectrum based on the Facies F2, F3 and F4 midpoint-triangle interpolated series. Dominant occur wavelengths at circa 1.7 -2.8 m, 5.2 m, 7.4 and 20-30 m

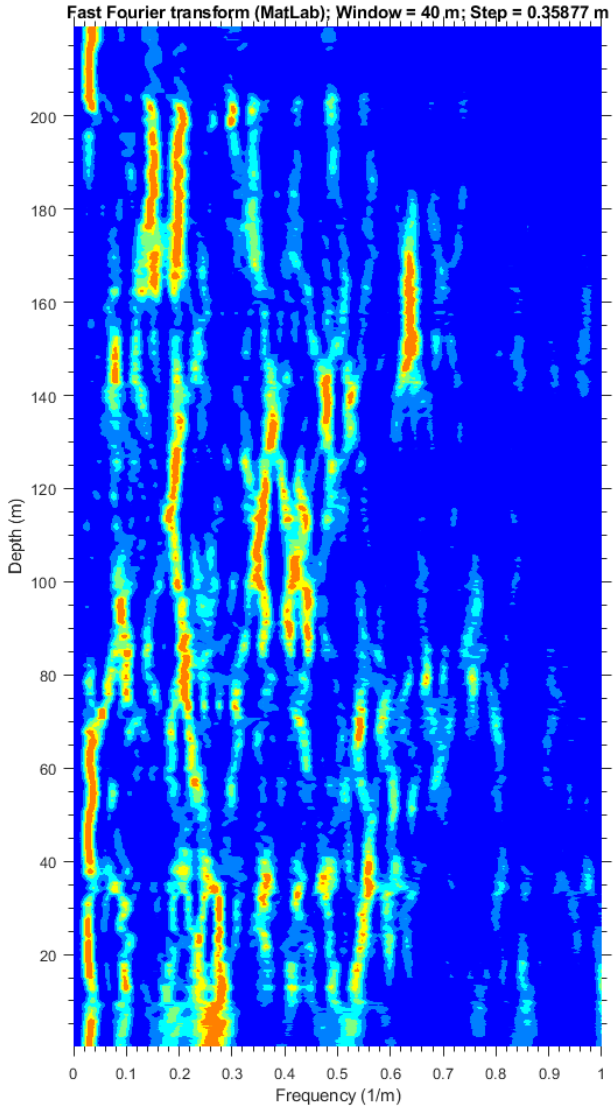

APPENDIX 1D4. Morlet wavelet spectrum based on the Facies F2, F3 and F4 midpoint-triangle interpolated series. Dominant wavelengths occur at circa 1.7 -2.8 m, 5.2 m, 7.4 m and 13 m

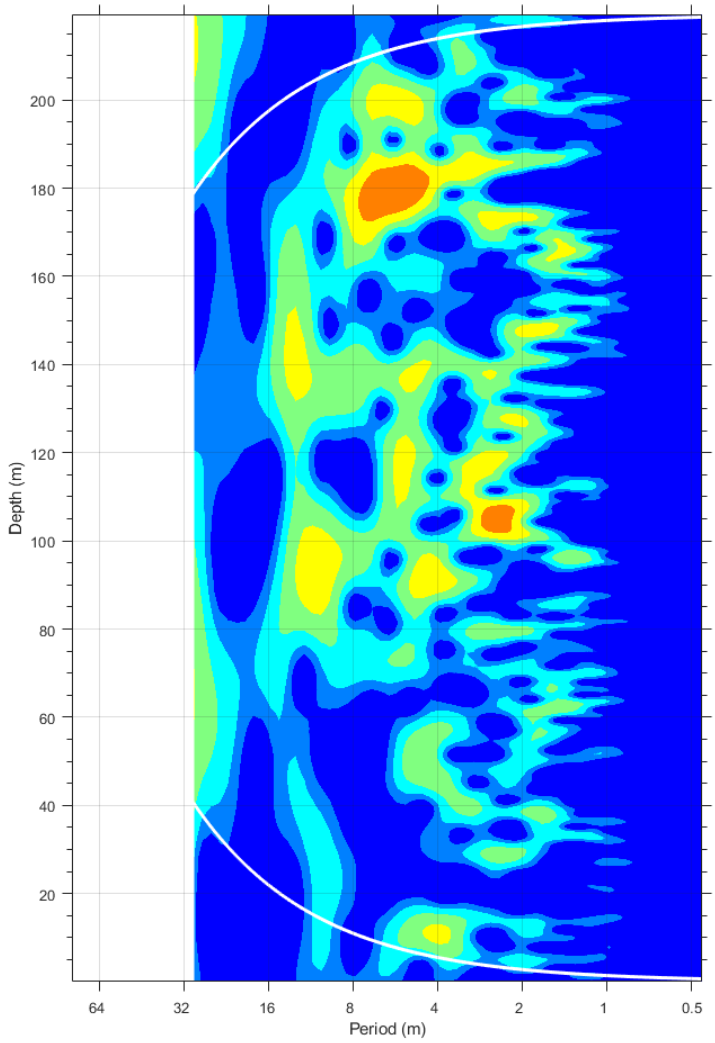

APPENDIX 1E. Results of TimeOpt analysis. Based on an integrated image displayed by all plots, the most probable average sedimentation rate is estimated at c. 6.5 cm/kyr